Back-propagating super-shear rupture in the 2016 *M*7.1 Romanche transform fault earthquake

Stephen P. Hicks[1,2], Ryo Okuwaki[3], Andreas Steinberg[4], Catherine Rychert[1], Nicholas Harmon[1], Rachel Abercrombie[5], Petros Bogiaztis[1], David Schlaphorst[6,7], Jiri Zahradnik[8], J-Michael Kendall[6,9], Yuji Yagi[3], Kousuke Shimizu[10], Henriette Sudhaus[4].

1. Department of Ocean and Earth Science, University of Southampton, United Kingdom.
2. Department of Earth Science and Engineering, Imperial College London, United Kingdom.
3. Faculty of Life and Environmental Sciences, University of Tsukuba, Japan.
4. Department of Geosciences, Christian-Albrechts-Universität, Kiel, Germany
5. Department of Earth and Environment, Boston University, United States
6. Department of Earth Science, University of Bristol, United States.
7. Faculdade de Ciências, Universidade de Lisboa, Lisbon, Portugal
8. Faculty of Mathematics and Physics, Charles University in Prague, Czech Republic.
9. Department of Earth Sciences, University of Oxford, United Kingdom.
10. Graduate School of Life and Environmental Sciences, University of Tsukuba, Japan.

Rupture propagation of an earthquake strongly influences potentially destructive ground shaking. Variable rupture behaviour is often caused by complex fault geometries, masking information on fundamental frictional properties. Geometrically smoother ocean transform fault (OTF) plate boundaries offer a favourable environment to study fault zone dynamics because strain is accommodated along a single, wide zone (up to 20 km width) offsetting homogeneous geology comprising altered mafic or ultramafic rocks. However, fault friction during OTF ruptures is unknown: no large (M_w>7.0) ruptures had been captured and imaged in detail. In 2016, we recorded an M_w 7.1 earthquake on the Romanche OTF in the equatorial Atlantic on nearby seafloor seismometers. We show that this rupture had two phases: (1) up and eastwards propagation towards the weaker ridge-transform intersection (RTI), then (2) unusually, back-propagation westwards at super-shear speed toward the fault's centre. Deep slip into weak fault segments facilitated larger moment release on shallow locked zones, highlighting that even ruptures along a single distinct fault zone can be highly dynamic. The possibility of reversing ruptures is absent in rupture simulations and unaccounted for in hazard assessments.

For large earthquakes, a variety of complex configurations of seismic slip have been proposed. These include cascading ruptures across multiple faults[1], including for intraplate ocean earthquakes[2] and closely-spaced doublets[3]. Such complexity, however, is dominated by pre-existing complex geometries of multiple fault segments[4]. In contrast, OTFs, which account for ~20% of the total length of global plate boundaries[5], have most strain accommodated along a single broad zone, a thermally controlled seismogenic width, and well-defined, ridge-controlled slip rates[6], making them the simplest realization of transform faults on earth. Their composition is likely to be strongly bi-material, controlled by plate age variation across the fault and hydrothermal alteration of mafic and ultramafic rocks[7]. The seismic behaviour of

OTFs was thought to be influenced by strongly-coupled discrete asperities[8–10], with short recurrence times of moderate earthquakes (M_w≤6.2) and aseismic transients along faster-slipping Pacific OTFs[11] allowing possible stable forecasting of OTF earthquakes[11–13]. The wide damage zone along OTFs[14] likely strongly affects seismogenic behaviour[10,15]. However, these concepts have yet to be explored for larger ruptures that occur along OTFs offsetting slower-spreading, Atlantic-type ridges[16].

Using only teleseismic data, past studies of OTF earthquakes suggested anomalously long rupture durations[16], with unilateral ruptures nucleating closer to the RTI, then propagating toward the centre of the fault[17–19]. Although fast strike-slip ruptures are found in continental[20], ocean-continent[21], and oceanic intraplate[2] settings, it remains unclear whether OTFs can host super-shear ruptures. OTF ruptures may be expected to be fast given their maturity[22], length, and linearity. Whilst OTFs offer a unique opportunity to investigate geological controls on rupture style and seismic cycle behaviour[15], to our knowledge, there has been no documented capture and analysis of large OTF earthquakes using nearby (i.e. <1,000 km) seafloor sensors.

Uniquely, in August 2016, an M_w 7.1 earthquake at the eastern end of the Romanche OTF in the central Atlantic Ocean was captured by a local ocean-bottom seismometer (OBS) network (**Figure 1**). The 920 km-long Romanche OTF is the second longest globally; large earthquakes along it are common, with 13 M_w 6.5+ events since 1970, including an M_w 7.1 rupture in 1994[17]. Using local OBS and teleseismic data of the earthquake and its aftershocks, we show that OTF earthquakes can have complex rupture at super-shear speeds and back-propagating fronts along a single fault. A simplified view using single-source hypocentre-centroid positions and delays[16] might have misinterpreted the 2016 Romanche earthquake as a slow rupture.

Rupture complexity from regional OBS and teleseismic recordings

The mainshock epicentre coincides with the 20-km wide Romanche axial valley, lying ~90 km WSW of the RTI (**Figure 1** & **Figure 2a**). The hypocentre depth is 20 km (±9 km) below sea level (BSL). The magnitude of the largest aftershock is M_L 4.8, consistent with the maximum aftershock magnitude decrement for OTF earthquakes globally of 2.2[6]. We find a high density of aftershocks ~20 km west of the mainshock epicentre, and some further east, up to 70 km away (**Figure 2a**). The aftershock distribution relative to the mainshock indicates a ~60-80 km-long bilateral rupture and hints at rupture asymmetry. Regional moment tensor (RMT) analysis (see **Methods**), using long-period waveforms that view the rupture as a point-source, shows strongly double-couple (98%) right-lateral strike-slip faulting along Romanche (**Figure 1**). The hypocentre-to-centroid time and epicentre shifts of 16 s and <20 km, respectively (**Figure 1**) imply a slow[16] rupture velocity, $v_r \approx 1$ km/s.

To investigate this apparent slow rupture, we inverted waveforms at shorter periods to solve for multiple sub-events with variable deviatoric RMTs[23] (see **Methods**). Waveform fits and source configurations are shown in **Figure 2** and described below. The largest pulse in the waveforms is reproduced by an M_w 6.9 sub-event at $\Delta t = 15$ s located within 6 km (±6 km) of the epicentre. We also fit a residual earlier pulse with an additional sub-event. This increases overall variance reduction by 20%, statistically significant with 95% confidence (**Note S4**). This M_w 6.6 sub-event ruptured earlier ($\Delta t = 10$ s) than the larger sub-event with its centroid lying 42 km (±6 km) east of the epicentre. We refer to the earlier, smaller sub-event as *SE1* and the later, larger sub-event as *SE2*. In contrast to early indications of a slow unilateral rupture, the location and timing of sub-events indicate a faster, complex rupture. The source-time

function reinforces this observation, similar to that from automated teleseismic analyses[24] (**Figure 2c**).

a) shows a low slip-rate (<2 cm/s) early on ($\Delta t = 0$–8 s), consistent with other large OTF earthquakes[17]. At $\Delta t = 8$–14 s, there is an emergent phase of slip rate (4 cm/s) ~35 km east of the hypocentre at shallow depth (SE1). Soon after, at $\Delta t > 16$ s, the rupture appears to travel west, toward, and beyond, the epicentre - rupturing a large asperity ~50 km long in the crust (SE2) with high slip-rate (7 cm/s).

Verification of rupture reversal

We find excellent consistency between the aftershock distribution, sub-event RMTs, and teleseismic slip inversion. Our observations suggest two rupture fronts propagating in opposite directions. There are two models that can explain this: (1) bilateral rupture with vastly different v_r in each direction; or (2) sequential back-propagating rupture with super-shear v_r.

Different rupture speeds in opposite directions were inferred for the 2013 M_w 7.5 Craig, Alaska earthquake with bilateral super- and sub-shear components[21]. If we assume a similar configuration for the Romanche earthquake, the larger asperity (SE2) would have ruptured very slowly ($v_r \approx 1$ km/s). Such a slow rupture might require a dissipative mechanism in ductile mantle[26], but the Romanche earthquake ruptured above the 800°C isotherm (**Figure 4**). Moreover, the teleseismic inversion fails to identify two simultaneous, antiparallel rupture fronts.

Alternatively, if the rupture changed direction following SE1, then this part of the rupture would have had to travel at super-shear speed ($v_r \approx 5$–6 km/s). To validate this model, we

used time-domain teleseismic back-projection (BP) imaging[27] with phase-weighted stacking (see **Methods**). The BP results (**Movie S1**) confirm an apparent reversal in rupture direction - from deeper rupture on a southerly-dipping fault to the westerly-travelling phase at shallow depth travelling at 4–6 km/s (**Figure 3b).**

We verify this result by searching for far-field Rayleigh Mach waves[28,29] using waveforms filtered at 10–20 s period from the Romanche mainshock with a co-located M_w 5.6 earthquake on 2018-02-15 with an identical mechanism[30] (**Figure 1**; see **Methods**). Between azimuths of 34–63° relative to rupture direction, many stations show high Rayleigh wave cross-correlation values of up to 0.98 between the mainshock and aftershock (**Figure 3c**; **Figure S14**). Accounting for phase velocity variations over large distances (**Figure S15**), these azimuths demarcate a Mach cone of lower directivity factor, similar to that predicted for a v_r of 5.7 km/s (see **Methods**; **Figure S15**). Outside the cone, waveform similarity is lower and typically does not exceed a cross-correlation coefficient 0.80 (**Figure 3c**; **Figure S14**). These observations rule out bilateral rupture with vastly differing v_r. A sharp change in rupture propagation direction along a single isolated fault has lacked precedence globally.

A remaining issue is whether, after nucleation ($\Delta t = 0$–9 s) the rupture front was continuous, or SE1 was dynamically triggered due to S-waves from rupture onset. The latter model, in which rupture nucleation may be regarded as a foreshock, is supported by the along-fault nodal maximum in S-wave amplitude[31] and apparent $v_r \approx 3.5$–4 km/s, close to the shear-wave velocity (v_S) of mid-to-lower crust. Yet OBS waveforms show continuous seismic energy radiation over time following rupture nucleation (**Figure S17**), supported by BP imaging. These observations favour a spreading rupture front, although we cannot completely rule out dynamic triggering mechanisms at smaller scales[32].

2-D segmentation in fault stress controls rupture propagation

The unique spatio-temporal evolution of the 2016 Romanche rupture adds new understanding to the geological controls on seismic slip along mature strike-slip faults, providing new evidence of super-shear rupture OTFs. Theoretical studies have suggested that inhomogeneous faults have preferred rupture directionality for sub- and super-shear rupture[38]. The segment that ruptured in 2016 is likely inhomogeneous since it offsets crust with an age difference of ~27 Ma (**Figure 1**). If we assume higher seismic velocities on the older and cooler north side, the preferred super-shear rupture direction[38] is east, opposite to observations. This finding indicates that rupture directionality might not be simply controlled by broad plate age/thermal variations. Instead, rupture direction may be more dependent on variable material properties within a wide fault zone[33]. More fracturing and/or serpentinisation may exist on the older side, possibly related to uplift of the transverse ridge to the north[34], which would reduce seismic velocity, and result in preferentially westward super-shear rupture.

The depth and lateral extent of rupture is likely determined by variations in serpentinisation in the seismogenic zone. The OBS data, teleseismic slip rate inversion and BP image deeper rupture initiation at ~20 km depth. Therefore, the rupture nucleated in the oceanic mantle, at the base of the seismogenic zone[6,35] between the 500–600°C isotherms (**Figure 4**). Nucleation was likely promoted by a stress increase due to the serpentine-to-peridotite transition where a change from velocity strengthening and weakening is expected to occur at low slip rates[6]. Most slip was in the crust, laterally extending beneath a topographically smoother segment of the Romanche axial valley (~6,200 m BSL; **Figure 2**, **Figure 4**). At the rupture's western end, a deeper valley (>6,500 m) (**Figure 2**, **Figure 4**) may highlight

hypothermal alteration and serpentinsation[13,32], restricting coupling and a barrier to seismic slip[32,34]. The eastern edge of the rupture lies where the seafloor steepens to shallower depths of <5,500 m (**Figure 4**), which likely restricted slip due to a narrowing seismogenic zone[35]. These bounding fault segments of the Romanche rupture are likely creeping zones that contribute to the overall low seismic coupling of OTFs[6].

Our preferred explanation for rupture reversal during the M_w 7.1 2016 Romanche earthquake is as follows and illustrated in **Figure 4**. Nucleation occurred at 20 km depth, above the brittle-ductile transition (**Figure 4** Step 1-2). SE1 then ruptured along the ~500°C isotherm towards the surface near the RTI, and was determined by transitional velocity-weakening altered and velocity-strengthening mantle peridotite[35] (**Figure 4**, Step 3-4). We speculate that the SE2 fault segment was pre-seismically more strongly coupled than that for SE1, but reactivation of it from a vertically propagating rupture front with little strain energy release was buffered by the altered mantle peridotite. Slip on SE1 then provided the rupture with enough strain energy release to overcome larger enough fracture energy in the locked SE2 segment, resulting in super-shear rupture and termination in an adjacent weak zone (**Figure 4**, Step 5-6). The transform fault may have had two highly stressed zones which promoted seismogenic failure[36] prior to the Romanche earthquake, or the deeper SE1 rupture instantaneously increased the static stress, immediately causing the shallow SE2 portion of the fault to fail.

Quantifying our proposed mechanism will require dynamic simulations of the rupture, along with detailed microseismic observations and seismic velocity images across OTFs. These will also verify whether transform plate boundaries may comprise parallel fault strands that may help to facilitate a reversing earthquake. Regardless of the exact model, we suggest that a cascading rupture reversal can occur when a weak nucleation phase starts in the mantle, and

away from a barrier on one side of the fault. Rupture directionality depends on interactions between the nucleation point, strain release history, and fracture energy variations along the fault. Whilst it has been suggested that seismogenic stresses on OTFs are more deterministic[6], our result implies that OTF earthquakes, even with long-lived asperity-barrier segmentation, may resemble those of continental strike-slip earthquakes, without requiring orthogonal fault systems.

A growing rupture in one direction may not be deterministic of a later emerging larger rupture travelling in the opposite direction, which may be important for earthquake early-warning systems. Also, this potentially limited understanding of seismic slip processes could result in underestimated near-field ground shaking amplitude and duration, which buildings and structures have to sustain during earthquakes.

Methods

Data: Local OBS network

We deployed 39 broadband OBS stations in March 2016 for twelve months as part of the PI-LAB (Passive Imaging of the Lithosphere-Asthenosphere Boundary) and the EURO-LAB (Experiment to Unearth the Rheological Oceanic Lithosphere-Asthenosphere Boundary) experiments (**Note S1**). The network centred on the Chain Fracture Zone, next to Romanche, provides good coverage of the eastern end of the Romanche OTF (**Figure S1**). Due to instrument issues at some stations, not all deployed components were used in this study.

Mainshock hypocentre and aftershock relocation

For hypocentre relocation, we used a 1-D layered P-wave velocity model for the central Atlantic from CRUST1.0[37], and a constant v_p/v_s ratio of 1.71 (See **Note S2**). We used the NonLinLoc package[38] for hypocentre relocations in which we employed a travel-time dependent error, which effectively gives an epicentral distance weighting. We used true depths below sea level of the OBS stations in the relocation. The epicentre lies NW of the PI-LAB OBS network, with the closest station 130 km away. Our epicentre is located <7 km away from those of other agencies that used teleseismic arrivals alone (**Table S1**), suggesting a robust estimation of the rupture nucleation position (**Figure S2**). Although the PI-LAB OBS network offers sub-optimal coverage of the rupture area, we are confident that the hypocentre locations are sufficiently accurate to probe the seismicity distribution along the fault (**Note S3**), although depths are poorly constrained. Next, we relocated 101 aftershocks and further refined these by performing a multiple-event relocation relative to the mainshock hypocentre (**Note S3**). We also scanned continuous waveforms at the closest three stations

to find any foreshocks in the days leading up to the mainshock, but we found none within this period along the Romanche Fracture Zone. Eleven of these aftershocks are in the USGS-NEIC catalogue.

RMT inversion

For RMT inversion, we computed Green's functions (GF) in our layered velocity model using the ortho-normal propagator method[39]. The GFs also incorporated an ocean layer 3.7 km thick, the mean station depth of the OBS network, with all receivers placed at this constant seafloor depth. We used the ISOLA software package[23] (see **Code Availability**), which inverts for waveforms in the time domain, to compute moment tensors. ISOLA searches across a prescribed grid of trial-point-sources to find the deviatoric CMT in space and time that maximises the fit (given as variance reduction; VR) between synthetic and observed waveforms. We carefully looked for waveforms unaffected by clipping and non-linear tilting due to the Romanche earthquake to stabilise solutions. We also tested the stability of inversion by jack-knifing waveform traces. We used stations located up to 700 km epicentral distance from the hypocentre of the Romanche mainshock; **Figure 1** shows the stations used for regional waveform inversion.

Based on initial CMT inversions, together with the mainshock hypocentre and the geometry of Romanche OTF from bathymetric data, we designed a grid of trial-point sources along a plane striking 75° and dipping 80° to the south-east. The origin of the plane is our relocated hypocentre. We placed 16 sources along-strike (spacing of 6 km), and 6 sources in the down-dip direction (spacing of 4 km).

We first inverted for a single-point source moment tensor solution using long-period waveforms (33–100 s period; **Figure S3).**

To investigate source complexity, we inverted waveforms at periods beyond the source corner frequency. We used iterative deconvolution, which has been used extensively to probe rupture complexity at regional scales[3,40,41]. For each sub-event, we searched for length of the triangular source-time function that maximised VR. The centroid location of SE1 is better constrained than that of SE2 (**Figure S4**). In the low-frequency waveforms, we do not find any significant pulse closer to the origin time, so we cannot robustly add a third sub-event, indicating comparatively less slip during the nucleation phase. This observation is in line with the 1994 Romanche earthquake[17].

To estimate an overall source-time function (STF) for the total rupture, we inverted the waveforms in terms of 10 s long equidistantly-shifted isosceles triangle functions and apply a non-negative least square constraint (NNLS)[42]. We prescribe the CMT parameters for both sub-events as per the result above and fix the total moment.

Teleseismic slip-rate inversion

Compared to an operational finite fault model for the 2016 Romanche earthquake from NEIC-USGS (https://earthquake.usgs.gov/earthquakes/eventpage/us20006uy6/finite-fault; last accessed December 2019), we found that a shallower, south-dipping fault substantially increased waveform fits at near-nodal stations.

We solved the spatio-temporal potency-density tensor distribution[25,43]. We represent slip along the fault with five-basis double-couple components so that we flexibly represent the slip vectors without forcing them to span an arbitrarily assumed model plane, which suppresses the modelling error due to the inappropriate assumption of the fault-plane geometry[25]. At every 1 s snapshot, the slip-rate function at each source node is represented by linear B-splines. Model parameters are objectively determined by minimising Akaike's

255 Bayesian Information Criterion (ABIC)[44], which is expected to produce solutions similar to fully
256 Bayesian inversions[45], since we do not adopt non-negative constraints for slip vectors
257 (positivity constraint) in our ABIC-based inversion scheme.

258 Vertical components of teleseismic P waveforms were downloaded from the Incorporated
259 Research Institutions for Seismology Data Management Center (IRIS DMC). We selected 51
260 stations (**Figure S5**) that cover all azimuths to capture radiation patterns and also chose
261 stations with high signal-to-noise ratio so we could reliably pick P-wave first motions. The
262 instrument responses were removed and the records were converted into velocity
263 waveforms, and then we resampled the data at 1.0 s. GFs were calculated with the near-
264 source velocity structures adopted from CRUST1.0[37]. We used the model plane striking at 79°
265 and dipping at 77° based on the procedure for our regional CMT inversion and the relocated-
266 aftershock distribution. The model plane was discretised into a grid spanning 10 km and 5 km
267 along the strike and dip directions, respectively. Our relocated hypocentre of the mainshock
268 was adopted for the initial rupture point. Guided by the position and timing of the sub-events
269 from RMT inversion, we set the total rupture duration as 30 s and the maximum rupture
270 speed at 6.0 km/s.

271 Synthetic tests and experiments using different fault-plane geometries produced a similar
272 pattern of slip to the optimum solution (**Notes S5 and S6**). The overall source-time function
273 also compares well with that derived from OBS waveforms (**Figure 2**c).We assessed the
274 robustness of the optimum teleseismic slip model by testing different fault geometries (up to
275 ±10° in strike and dip). In all fault geometry configurations, the overall pattern of the slip
276 distribution is very similar to that of the optimum model (**Note S5**). We also forward modelled
277 waveforms from our optimum smooth solution, added Gaussian noise of 1% of the signal

variance, and inverted these waveforms. This synthetic test (**Figure S12**) shows that the inversion is able to retrieve the predominate features of the rupture in space and time.

In raw teleseismic P-waves (**Figure S5**) small pulses following the initial P-wave are visible, with a broad pulse at $\Delta t = 10$ s (SE1) particularly clear at WSW and ESE azimuths. This is followed by a larger pulse at $\Delta t = 20$ s (SE2). **Figure S5** shows the resulting teleseismic P-wave fits for our best-fitting model. The P-wave azimuthal variation of low-frequency teleseismic P-waves confirms that the larger slip patch (SE2) occurred west of the rupture nucleation (**Figure S6**).

Teleseismic back-projection imaging

We used the Palantiri software (see **Code Availability**) which clusters stations at teleseismic distances and generates virtual seismic arrays[27,46]. We calculate the travel-times between grid-points and stations using the ak135 velocity model and stack in 12 s long moving windows (centred on each timestep) with respect to the expected P-wave onsets using the phase-weighted method[47]. We stack waveforms with respect to normalised semblance, which is a measure of the fraction of the radiated energy released as coherent waves. Semblance has sharper resolution than beampower for low-energy radiation and is less sensitive to amplitude effects due to site terms. The semblance from all virtual arrays is combined at each 3 s timestep for a total duration of 30 s (10 timesteps). To avoid an azimuthal bias, we subdivide all azimuthal directions around the epicentre into twelve sectors. The semblance from each azimuth sector is normalized to one, so that each azimuthal sector has the same influence on the combined semblance.

Bayesian bootstrapping of array weights is used to estimate the significance of the estimated location of the semblance. This means that the semblance is combined 100 times with

randomised Bayesian weights for each array and with slightly perturbed velocity models such that arrival times may vary by +/- 4s.

In total, 345 stations from IRIS, GEOFON and RESIF data centers are clustered using the *k*-means algorithm into 27 virtual arrays with a maximum aperture of 5° (**Figure S13**). We use velocity waveform recordings down-sampled to 10 Hz and to investigate the high-frequency emissions we bandpass filter between 0.2 Hz and 1.5 Hz. Stations which waveforms have a correlation coefficient <0.6 relative to the centremost station of each virtual array are blacklisted. We carried out the back-projection on two planar grids: one at 2.5 km depth and the other at 10 km depth below the seafloor. For the nucleation phase, we find a higher coherence of back-projected waves using the 10 km depth grid, consistent with rupture initiation at depth (**Figure3b**). However, for the overall rupture, the shallower grid results in higher waveform coherence, consistent with rupture at crustal levels.

Rayleigh wave Mach cone analysis

Past theoretical and applied studies[28,29] have shown that the effect of rupture directivity on surface waves can be used to determine rupture velocity. For earthquakes rupturing at velocities below seismic wave speed, waves from the start and end of rupture arrive at a far-field receiver at variable times. However, for super-shear earthquakes, at stations located on the Mach cone, the waves from different parts of the rupture arrive at the same time. These simultaneous arrivals result in surface waveforms that are highly correlated with those of a smaller, co-located earthquake with identical faulting mechanism that can be viewed as a point-source at the periods considered.

The range of azimuths where high waveform correlation can be observed depends on several factors: rupture direction, speed and duration, Rayleigh wave velocity, and frequency band.

Given the source duration of SE2 of ~25 s (**Figure 2c**), we can only see a significant azimuthal variation in directivity factor at frequencies above the corner frequency. Therefore, we bandpass filter waveforms between 10 s and 20 s period. We estimate Rayleigh wave phase velocities from the GDM52 model[48]. GDM52 gives velocities at a minimum period of 25 s – a longer period than that of our filtered waveforms; given the large variation in velocities along the long surface wave paths (typically 40–80° distance; **Figure S15**), we choose a mean surface wave velocity of 3.4 km/s for the shorter periods considered in this study. Taking a short-period cut-off filter corner at 10 s, and assuming a mean along-path Rayleigh wave phase velocity of 3.4 km/s, we predict a high waveform similarity - i.e. a small directivity factor - between the azimuths of 34–69° with respect to the rupture direction (**Figure S16**).

Our Rayleigh wave Mach Cone analysis for the 1994 M_w 7.1 Romanche earthquake[17] also hints at super-shear rupture (**Figure S18**).

Data availability

Continuous raw seismic waveform data from the PI-LAB ocean bottom seismometer network is available to download from IRIS Data Management Center (https://doi.org/10.7914/SN/XS_2016).

Continuous raw seismic waveform data from various global seismic networks used for the slip-rate inversion, back-projection and Mach cone analysis is available to download from IRIS Data Management Center.

Code availability

- The ISOLA software used for RMT inversion is available from http://geo.mff.cuni.cz/~jz/for_Cuba2018/.
- The Palantiri software used for teleseismic back-projection analysis is available from https://braunfuss.github.io/Palantiri/.

Figures

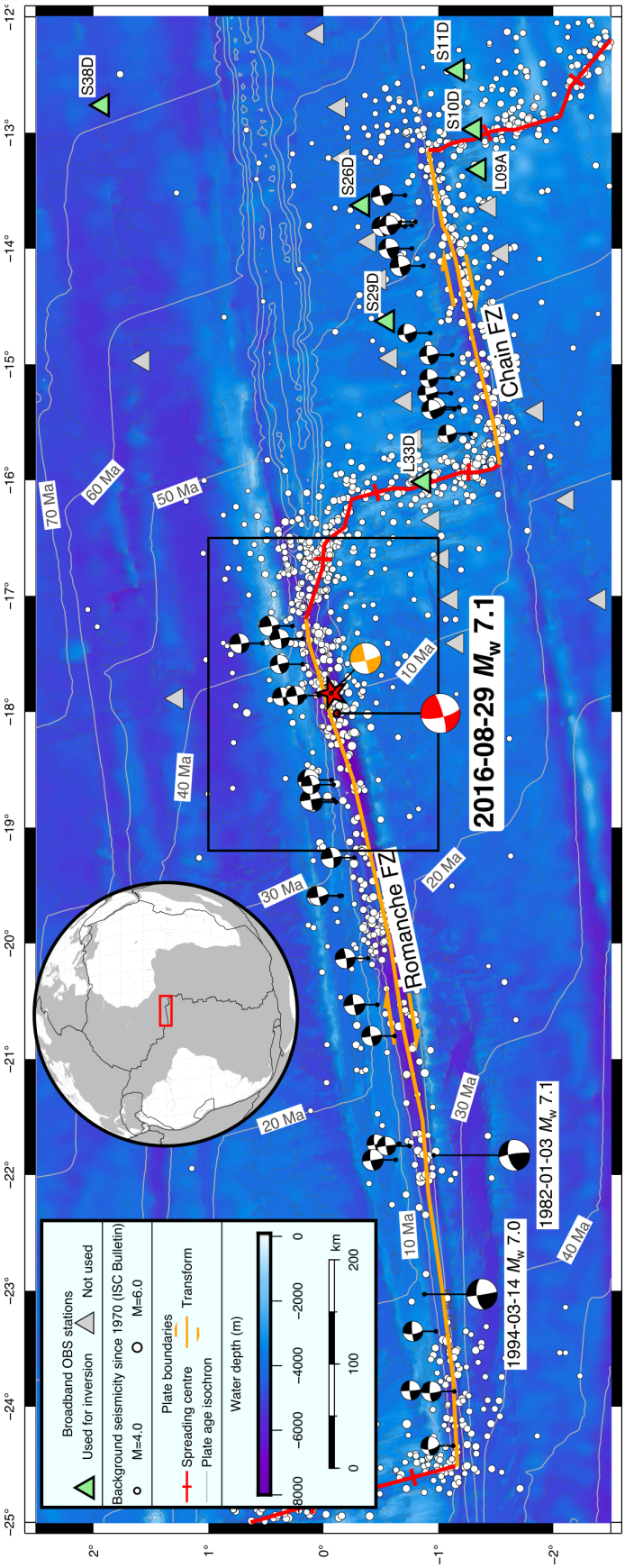

Figure 1: Seismo-tectonic context of the 2016 Romanche earthquake. Location of the map is given by the red rectangle on the globe. Bathymetry data comes from multi-beam swath bathymetry taken during the 2016 PI-LAB expedition and from the GEBCO atlas. Focal mechanisms are shown for M_w>6 events[30]. Stations from the PI-LAB experiment that were used for the waveform inversion are shown as dark blue triangles; other stations used for hypocentre relocation are shown as grey triangles. M_w>7.0 events are indicated by larger beach balls. Our relocated hypocentre and low-frequency RMT of the 2016 Romanche earthquake are shown by the red star and red beach ball, respectively. The orange beach ball is a co-located M_w 5.8 used for Mach cone analysis. The black rectangle shows the location of map in **Figure 2**.

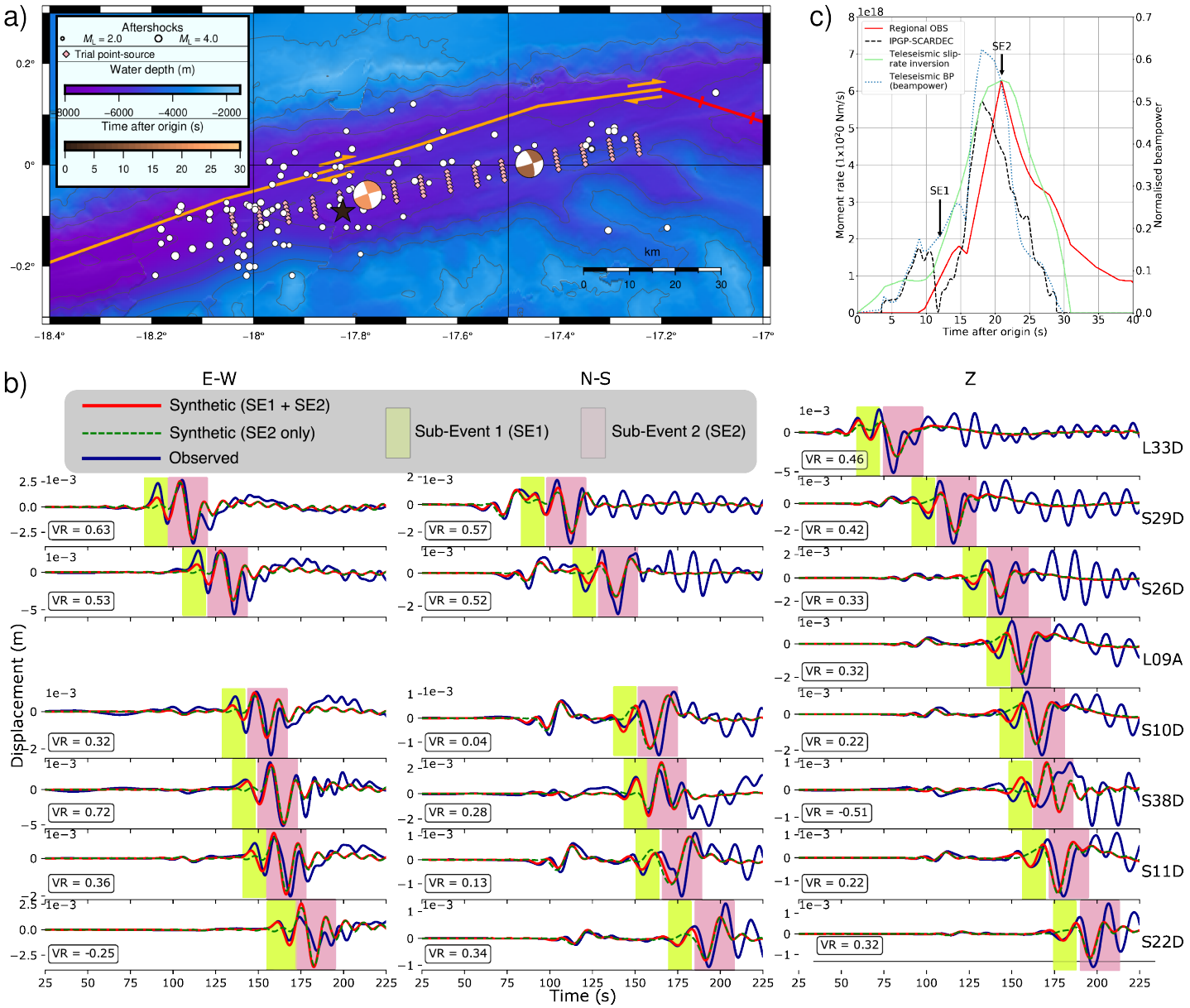

Figure 2: Results of the multiple-point source CMT inversion using regional OBS waveforms. a) Detailed bathymetry map of the hypocentral area of the 2016 M_w 7.1 Romanche earthquake showing aftershock epicentres and sub-event RMTs (beach balls; coloured by centroid time). The grid of trial-point sources for regional multi-source CMT inversion is shown. The mainshock hypocentre is shown by the star. Plate boundaries labelled as in **Figure 1**. b) Waveform fits for the multi-point source CMT inversion for all traces used, with shading to show the two pulses from both sub-events. The waveform fit using one sub-event only is also shown. The overall variance reduction (VR) is shown in the bottom left of each panel. Horizontal components for L33D and L09A were removed due to clipping or non-linear tilt effects due to the earthquake. c) Total moment rate function using regional waveforms parameterized as 1 s shifted triangular sources with 10 s length (solid red line), compared with an automated teleseismic estimate[24] and that from the teleseismic slip-rate inversion and back-projection (BP) of this study. Sub-event centroid times are labelled.

350

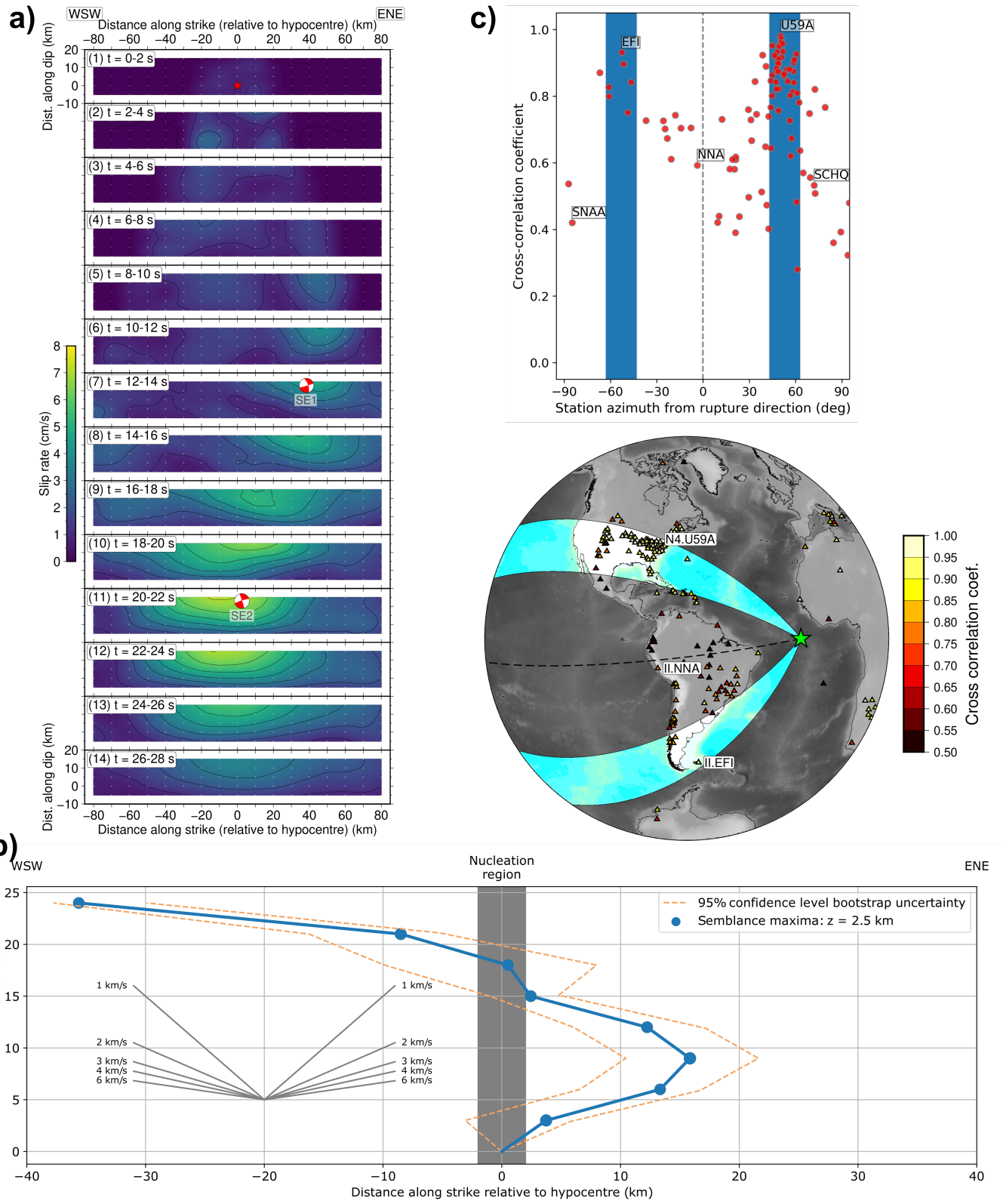

Figure 3: Teleseismic rupture analyses. a) Evolution of slip rate over time along the fault, given in two-second interval steps (labelled in the top-left corner), from inversion of teleseismic P-waves. Grey lines indicate contours of constant rupture velocity. b) Along-strike position relative to the hypocentre and timing of high-frequency radiators (circles scaled by semblance maxima values), and estimated uncertainty, sampled at 3 s time-steps (blue circles). Reference slopes are given in grey for different rupture velocities. c) Results from Rayleigh wave Mach cone analysis. Map showing cross-correlation coefficient values at each station (top), and plot showing the azimuthal variation in cross-correlation coefficient (bottom). The coloured region indicates the estimated Mach cone area. Waveforms from labelled stations are shown in **Figure S13**.

351

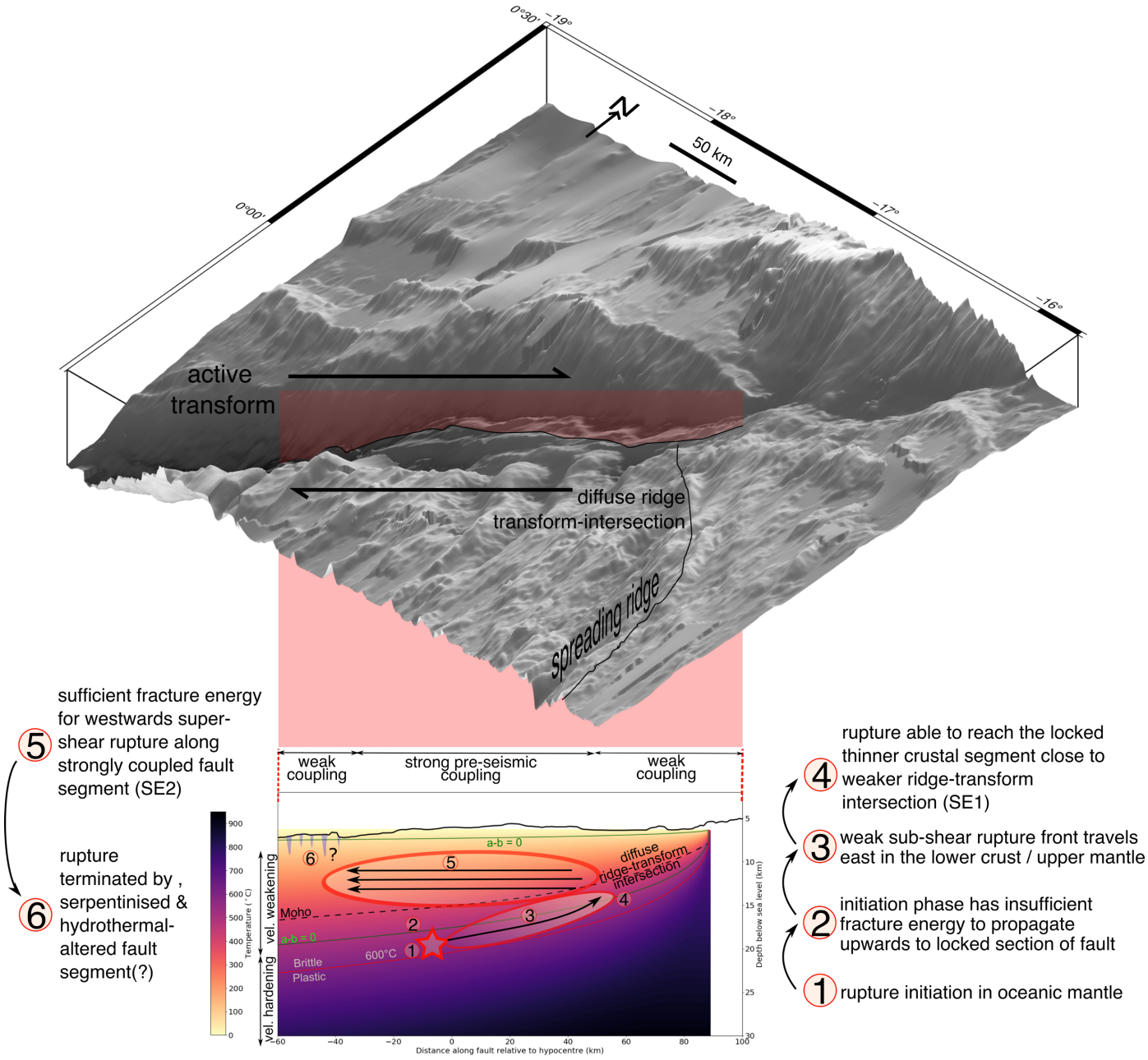

Figure 4: Our interpretation of the rupture geometry and processes of the 2016 Romanche earthquake. Top: perspective view with bathymetry of the study area. Bottom: cut through along the ruptured fault plane. Colours show a thermal profile based on half-space cooling and rate-/state-frictional regimes from Gabbro data[35]. Key stages of the rupture evolution are shown and annotated.

352

References

1. Zhang, H., Koper, K. D., Pankow, K. & Ge, Z. Imaging the 2016 Mw 7.8 Kaikoura, New Zealand, earthquake with teleseismic P waves: A cascading rupture across multiple faults. *Geophys. Res. Lett.* **44**, 4790–4798 (2017).

2. Meng, L. *et al.* Earthquake in a Maze: Compressional Rupture Branching During the 2012 Mw 8.6 Sumatra Earthquake. *Science* **337**, 724 726 (2012).

3. Hicks, S. P. & Rietbrock, A. Seismic slip on an upper-plate normal fault during a large subduction megathrust rupture. *Nat. Geosci.* **8**, 955 960 (2015).

4. Ross, Z. E. *et al.* Hierarchical interlocked orthogonal faulting in the 2019 Ridgecrest earthquake sequence. *Science* **366**, 346–351 (2019).

5. Bird, P. An updated digital model of plate boundaries. *Geochem. Geophys. Geosystems* **4**, (2003).

6. Boettcher, M. & Jordan, T. Earthquake scaling relations for mid-ocean ridge transform faults. *J. Geophys. Res.* **109**, 74 (2004).

7. White, R., Detrick, R., Sinha, M. & Cormier, M. Anomalous seismic crustal structure of oceanic fracture zones. *Geophys. J. Int.* **79**, 779–798 (1984).

8. Kuna, V. M., Nábělek, J. L. & Braunmiller, J. Mode of slip and crust–mantle interaction at oceanic transform faults. *Nat. Geosci.* **12**, 138 (2019).

9. Sykes, L. R. & Ekström, G. Earthquakes along Eltanin transform system, SE Pacific Ocean: fault segments characterized by strong and poor seismic coupling and implications for long-term earthquake prediction. *Geophys. J. Int.* **188**, 421 434 (2012).

10. Froment, B. *et al.* Imaging along-strike variations in mechanical properties of the Gofar transform fault, East Pacific Rise. *J. Geophys. Res.* **119**, 7175 7194 (2014).

11. McGuire, J. J., Boettcher, M. S. & Jordan, T. H. Foreshock sequences and short-term earthquake predictability on East Pacific Rise transform faults. *Nature* **434**, 457 461 (2005).

12. McGuire, J. Seismic Cycles and Earthquake Predictability on East Pacific Rise Transform Faults. *B. Seismol. Soc. Am.* **98**, 1067–1084 (2008).

13. Roland, E. & McGuire, J. J. Earthquake swarms on transform faults. *Geophys. J. Int.* **178**, 1677–1690 (2009).

14. Avendonk, V. H., Harding, A., Orcutt, J. & McClain, J. Contrast in crustal structure across the Clipperton transform fault from travel time tomography. *J. Geophys. Res.* **106**, 10961 10981 (2001).

15. Schwehr, M., Boettcher, M. S., McGuire, J. J. & Collins, J. A. The relationship between seismicity and fault structure on the Discovery transform fault, East Pacific Rise. *Geochem. Geophys. Geosystems* **15**, 3698 3712 (2014).

16. Duputel, Z., Tsai, V. C., Rivera, L. & Kanamori, H. Using centroid time-delays to characterize source durations and identify earthquakes with unique characteristics. *Earth. Planet. Sci. Lett.* **374**, 92–100 (2013).

17. Abercrombie, R. E. & Ekström, G. Earthquake slip on oceanic transform faults. *Nature* **410**, 74 77 (2001).

18. Antolik, M., Abercrombie, R. E., Pan, J. & Ekström, G. Rupture characteristics of the 2003 Mw 7.6 mid-Indian Ocean earthquake: Implications for seismic properties of young oceanic lithosphere. *J. Geophys. Res.* **111**, B04302 (2006).

19. Aderhold, K. & Abercrombie, R. E. The 2015 Mw 7.1 earthquake on the Charlie-Gibbs transform fault: Repeating earthquakes and multimodal slip on a slow oceanic transform. *Geophys. Res. Lett.* **43**, 6119-6128

(2016).

20. Wang, D., Mori, J. & Koketsu, K. Fast rupture propagation for large strike-slip earthquakes. *Earth. Planet. Sci. Lett.* **440**, 115 126 (2016).

21. Yue, H. *et al.* Supershear rupture of the 5 January 2013 Craig, Alaska (Mw 7.5) earthquake. *J. Geophys. Res.* **118**, 5903-5919 (2013).

22. Huang, Y., Ampuero, J.-P. & Helmberger, D. V. The potential for supershear earthquakes in damaged fault zones – theory and observations. *Earth. Planet. Sci. Lett.* **433**, 109–115 (2016).

23. Sokos, E. N. & Zahradnik, J. ISOLA a Fortran code and a Matlab GUI to perform multiple-point source inversion of seismic data. *Comput. Geosci.* **34**, 967 977 (2007).

24. Vallée, M., Charléty, J., Ferreira, A., Delouis, B. & Vergoz, J. SCARDEC: a new technique for the rapid determination of seismic moment magnitude, focal mechanism and source time functions for large earthquakes using body-wave deconvolution. *Geophys J. Int.* **184**, 338 358 (2011).

25. Shimizu, K., Yagi, Y., Okuwaki, R. & Fukahata, Y. Development of an inversion method to extract information on fault geometry from teleseismic data. *Geophys. J. Int.* **220**, 1055–1065 (2020).

26. Prieto, G. A., Froment, B., Yu, C., Poli, P. & Abercrombie, R. Earthquake rupture below the brittle-ductile transition in continental lithospheric mantle. *Sci. Adv.* **3**, e1602642 (2017).

27. Krüger, F. & Ohrnberger, M. Tracking the rupture of the Mw = 9.3 Sumatra earthquake over 1,150 km at teleseismic distance. *Nature* **435**, 937–939 (2005).

28. Vallée, M. & Dunham, E. Observation of far-field Mach waves generated by the 2001 Kokoxili supershear earthquake. *Geophys. Res. Lett.* **39**, L05311 (2012).

29. Bao, H. *et al.* Early and persistent supershear rupture of the 2018 magnitude 7.5 Palu earthquake. *Nat. Geosci.* **12**, 200–205 (2019).

30. Ekström, G., Nettles, M. & Dziewoński, A. The global CMT project 2004–2010: Centroid-moment tensors for 13,017 earthquakes. *Phys. Earth. Planet. Int.* **200**–**201**, 1–9 (2012).

31. Wang, D., Mori, J. & Uchide, T. Supershear rupture on multiple faults for the Mw 8.6 Off Northern Sumatra, Indonesia earthquake of April 11, 2012. *Geophys. Res. Lett.* **39**, L21307 (2012).

32. Roland, E., Lizarralde, D., McGuire, J. J. & Collins, J. A. Seismic velocity constraints on the material properties that control earthquake behavior at the Quebrada-Discovery-Gofar transform faults, East Pacific Rise. *J Geophys. Res.* **117**, B11102 (2012).

33. Xia, K., Rosakis, A. J., Kanamori, H. & Rice, J. R. Laboratory Earthquakes Along Inhomogeneous Faults: Directionality and Supershear. *Science* **308**, 681–684 (2005).

34. Bonatti, E. *et al.* Transform migration and vertical tectonics at the Romanche fracture zone, equatorial Atlantic. *J. Geophys. Res.* **99**, 21779-21802 (1994).

35. Liu, Y., McGuire, J. J. & Behn, M. D. Frictional behavior of oceanic transform faults and its influence on earthquake characteristics. *J. Geophys. Res.* **117**, B04315 (2012).

36. Michel, S., Avouac, J.-P., Lapusta, N. & Jiang, J. Pulse-like partial ruptures and high-frequency radiation at creeping-locked transition during megathrust earthquakes. *Geophys. Res. Lett.* **44**, 8345–8351 (2017).

37. Laske, G., Masters, G., Ma, Z. & Pasyanos, M. Update on CRUST1. 0—A 1-degree global model of Earth's crust. *Geophys. Res. Abstr* **15**, 2658 (2013).

468 38. Lomax, A., Virieux, J., Volant, P. & Berge-Thierry, C. Probabilistic Earthquake Location in 3D and Layered
469 Models. *Advances in Seismic Event Location* **18**, 101-134 (2000).
470
471 39. Wang, R. A simple orthonormalization method for stable and efficient computation of Green's functions.
472 *Bull. Seismol.l Soc. Am.* **89**, 733-741 (1999).
473
474 40. Bie, L., Hicks, S., Garth, T., Gonzalez, P. & Rietbrock, A. 'Two go together': Near-simultaneous moment
475 release of two asperities during the 2016 Mw 6.6 Muji, China earthquake. *Earth Planet. Sci. Lett.* **491**, 34-42
476 (2018).
477
478 41. Zahradník, J. *et al.* A recent deep earthquake doublet in light of long-term evolution of Nazca subduction.
479 *Sci. Rep.* **7**, 45153 (2017).
480
481 42. Zahradnik, J. & Sokos, E. N. The Mw 7.1 Van, Eastern Turkey, earthquake 2011: two-point source modelling
482 by iterative deconvolution and non-negative least squares. *Geophys. J. Int.* **196**, 522 538 (2014).
483
484 43. Yagi, Y. & Fukahata, Y. Introduction of uncertainty of Green's function into waveform inversion for seismic
485 source processes. *Geophys. J. Int.* **186**, 711-720 (2011).
486
487 44. Yabuki, T. & Matsu'ura, M. Geodetic data inversion using a Bayesian information criterion for spatial
488 distribution of fault slip. *Geophys. J. Int.* **109**, 363–375 (1992).
489
490 45. Fukuda, J. & Johnson, K. A Fully Bayesian Inversion for Spatial Distribution of Fault Slip with Objective
491 Smoothing. *B. Seismol. Soc. Am.* **98**, 1128-1146 (2008).
492
493 46. Roessler, D., Krueger, F., Ohrnberger, M. & Ehlert, L. Rapid characterisation of large earthquakes by
494 multiple seismic broadband arrays. *Nat. Hazards Earth Syst. Sci.* **10**, 923–932 (2010).
495
496 47. Schimmel, M. & Paulssen, H. Noise reduction and detection of weak, coherent signals through phase-

497 weighted stacks. *Geophys J. Int.* **130**, 497–505 (1997).

498

499 48. Ekström, G. A global model of Love and Rayleigh surface wave dispersion and anisotropy, 25–250 s.

500 *Geophys J. Int.* **187**, 1668–1686 (2011).

Supplementary information to "Back-propagating super-shear rupture in the 2016 *M*7.1 Romanche transform fault earthquake" by Stephen Hicks et al.

Contents of this document

Supplementary Notes

S1 Details of the PI-LAB ocean-bottom seismometer network

The OBS network (**Figure S1**) comprised a mixture of OBS packages with three-component seismometers. Instruments came from Lamont-Doherty (120 s long-period response), Institut de Physique du Globe de Paris (120 s long-period response) and Scripps Institute of Oceanography (240 s long-period response). We computed the azimuths of horizontal seismometer components using automatic Rayleigh-wave polarisation analysis[1] and each station comprised a hydrophone or differential pressure gauge (DPG), used for constraining P-wave arrival times.

S2 Velocity model, arrival time picking and mainshock relocation

We chose a constant v_p/v_s of 1.71, which is consistent with reduced Wadati plot regression, and resulted in epicentres clustering along the surface trace of the Romanche OTF. A v_p/v_s ratio is also consistent with shear-wave velocity information from surface wave tomography (Rychert et al., in Review). Using a variable v_p/v_s ratio from CRUST1.0 resulted in more scattered hypocentre locations and unstable CMT solutions. The velocity model does not contain a sediment layer as <80 m thick sediment layers have been inferred for the deployment area[2].

We manually picked P-and S-wave arrivals at OBS stations, simultaneously solving for locations, using the SDX software[3]. We relocated the hypocentres using NonLinLoc[4]. The posterior probability density function offers a complete probabilistic solution to the earthquake location problem, including information on uncertainty and resolution. The

closest OBS station is 120 km from the Romanche mainshock and the events lie outside the network (mean minimum azimuthal gap of 260°). However, assuming a homogeneous seismic velocity structure in oceanic plates, we believe the epicentral locations are robust. The low root-mean-square residual between theoretical and observed arrivals (RMS) for all events of <0.50 s supports this assumption as the furthest stations are >1,000 km away. The known strike of the fault, together with the fault-parallel azimuth of minimum axis epicentral uncertainty ellipse (**Figure S2**), due to the network geometry, gives us a robust constraint on the rupture extent. To ensure that our location estimate was not biased by the possibility of S-wave arrival times mis-picked due to rupture complexity, we computed the hypocentre using P-waves arrivals alone, which produce a similar location.

S3 Aftershock detection, catalogue and relocation

We formed a catalogue of aftershocks by first picking and analysing events in the ISC Bulletin in the region for three months after the mainshock. Additionally, we also took automatic local event detections from the PILAB experiment (Schlaphorst, in Prep.) based on the cluster-search algorithm of the SeisComp3 analysis package[5]. Due to the lack of station coverage, this automatic detection approach only captured a subset of the largest aftershocks; therefore, we also scanned continuous waveforms from the closest three stations (L02A, L33D, I34D) to detect aftershocks until 60 days after the mainshock. Overall, we relocated 101 events with well-constrained locations (RMS residual <0.8; maximum azimuthal gap < 270). To provide a greater precision of aftershock epicentres, we then used the BayesLoc software[6] to perform a multiple-event relocation. We used all available local data from ocean-bottom seismometers and available teleseismic P arrivals from the ISC Bulletin. Then we performed a relative relocation by fixing the location of the mainshock and prescribing looser constraints

on the aftershock origins based on the standard errors from NonLinLoc. Hypocentre depths of aftershocks remain very poorly constrained. Local magnitudes were computed using a generic M_L scale for California[7]. We find a good correlation between M_L, M_b, and M_w for the larger aftershocks. We recorded aftershocks with M_L = 3.0 to M_L = 4.8.

S4 Statistical significance of two sub-events in RMT inversion

We assess the statistical significance of the second sub-event using an F-test[8]. We assume that samples are correlated over a period corresponding to the low-pass filter corner used in the inversion (10 s), and the dominant part of each waveform is ~150 s long, yielding 15 independent samples per component. For all 20 components (i.e. 300 data points) and subtracting the number of free parameters for a deviatoric moment tensor (7), we find that the increase in waveform fit is significant at the 98% confidence level.

S5 Teleseismic inversion, sensitivity test with variant configuration of model-plane geometry

Figure S7 shows a comparison of the resulting slip models using different inversion schemes. The effect of using different inversion schemes is shown (**Figure S8**, **Figure S9**, **Figure S10**, **Figure S11**) for different assumptions on the model fault geometry (see paragraph below for details). In each figure, Panel (a) shows the results of the conventional inversion scheme[9] with the double-couple components of the shear plane of each sub-fault patch constrained by the model plane. Figures in Panel (b) are the results from the preferred inversion scheme without forcing the shear plane to be the model plane, which we adopted in our study. As shown, there are systematic differences between the fixed and the non-fixed models. The key

feature, however, of a long initial rupture stage followed by the main rupture propagating from east to west is resolved from both approaches.

We also tested the effect of unknown model-plane geometry by adding fluctuations of ±10° ±5° in strike and dip from the optimum model (strike: 79°; dip: 77°); (**Figure S8**, **Figure S9**, **Figure S10**, **Figure S11**). As shown, the fixed models are not stable against the assumption of the model-plane geometry, especially when dip angle is varied. In general, especially for the strike-slip earthquakes like the 2016 Romanche earthquake, the radiation pattern is sensitive to the nodal plane orientations, and the pre-fixed model-plane geometry may violate the solution since it cannot resolve small subtle changes in faulting geometry, even on an ocean transform fault. In contrast, the non-fixed models are relatively robust against the model-plane geometry, and the overall slip evolution is obtained in all the models.

S6 Teleseismic inversion, synthetic test with forward-modelled waveforms

We performed a synthetic test of the teleseismic inversion. Synthetic waveforms were generated by using the slip distribution of the optimum model. We added the Gaussian noise with zero mean and 1% variance to the dataset, and then we inverted the synthetic waveforms to investigate whether we could retrieve the solution. As shown in **Figure S12**, the synthetic test properly retrieves the input model, although slight change of the peak slip and the focal mechanism can be seen.

Supplementary Figures

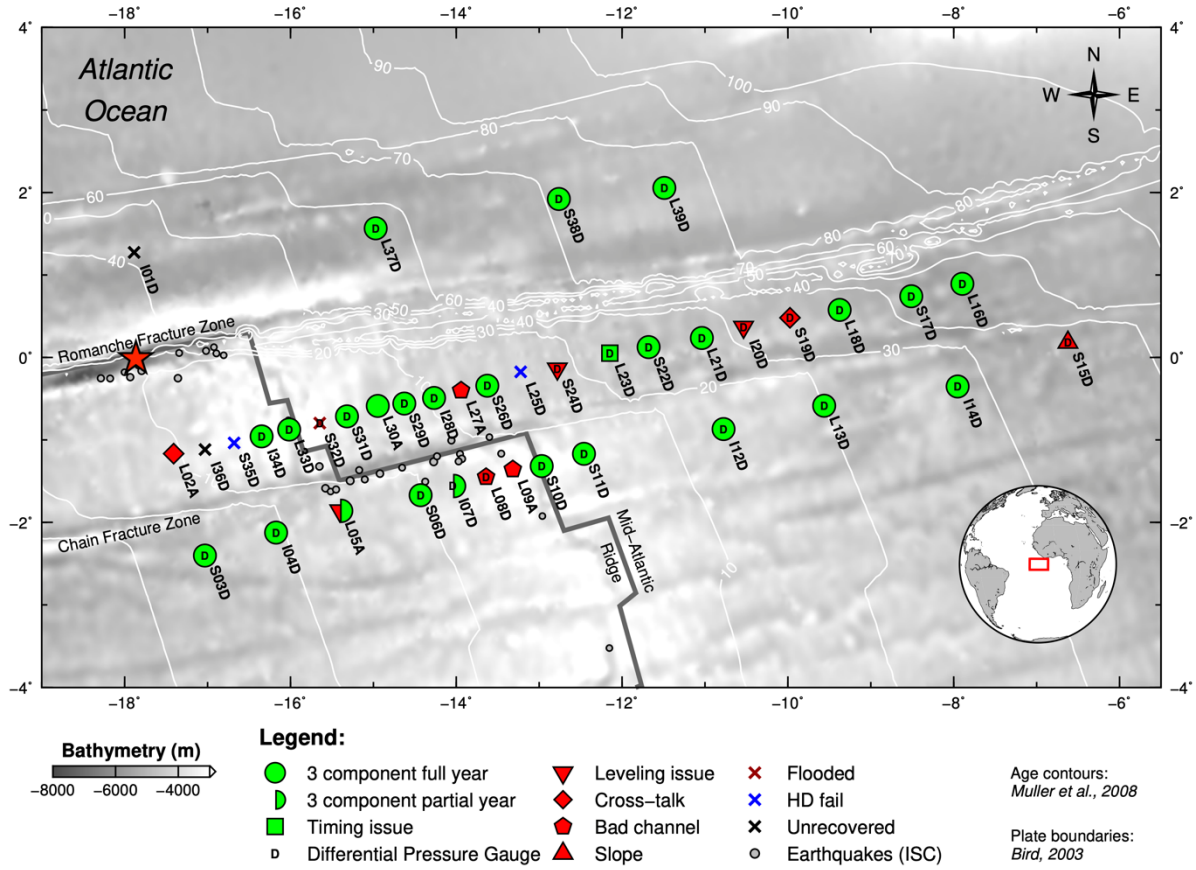

Figure S1: Full network map of the PI-LAB ocean-bottom seismometer deployment. All available stations were used for mainshock and aftershock sequence relocations. Stations are coloured according to instrument performance and data recovery. The red star gives the epicentre of the 2016 Romanche earthquake.

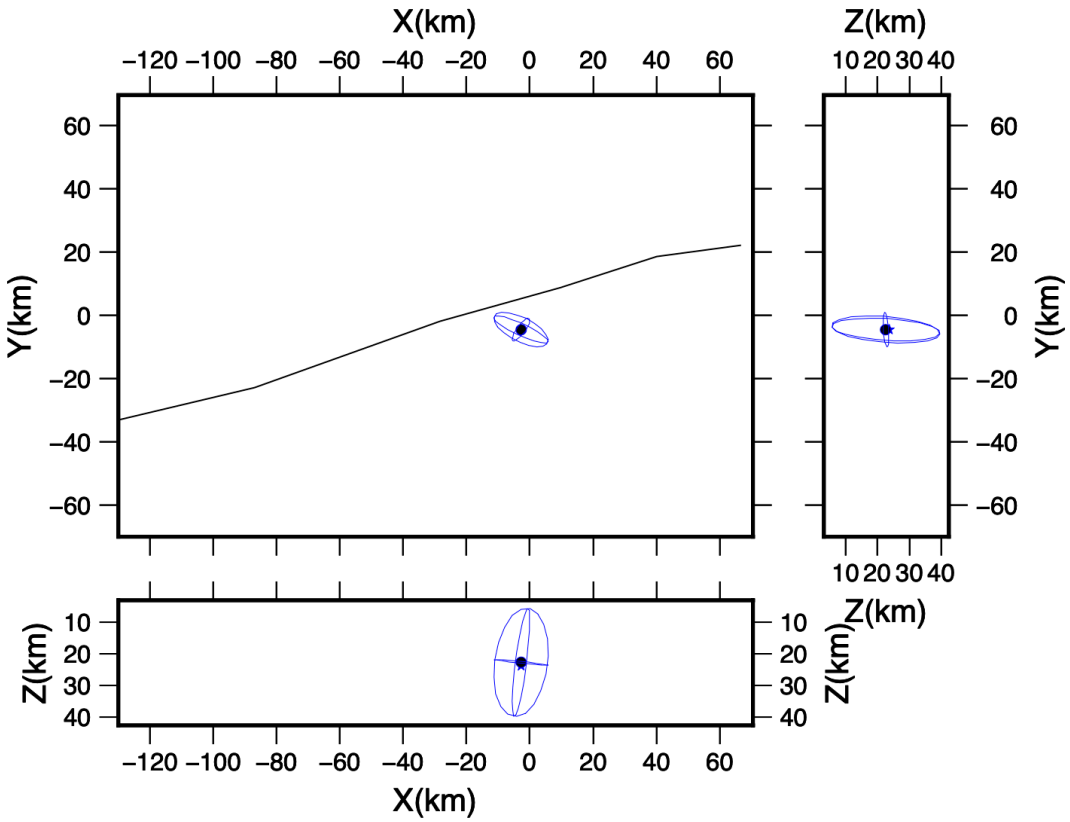

Figure S2: 68% confidence ellipsoid estimate for our relocated hypocentre of the Romanche earthquake projected in map view (top-left); the X-Z plane (bottom-left) and the Y-Z plane (top-right). The dot shows the Gaussian expected hypocentre and the star shows the maximum likelihood hypocentre estimate. The black line shows the approximate position of the Romanche Fracture Zone.

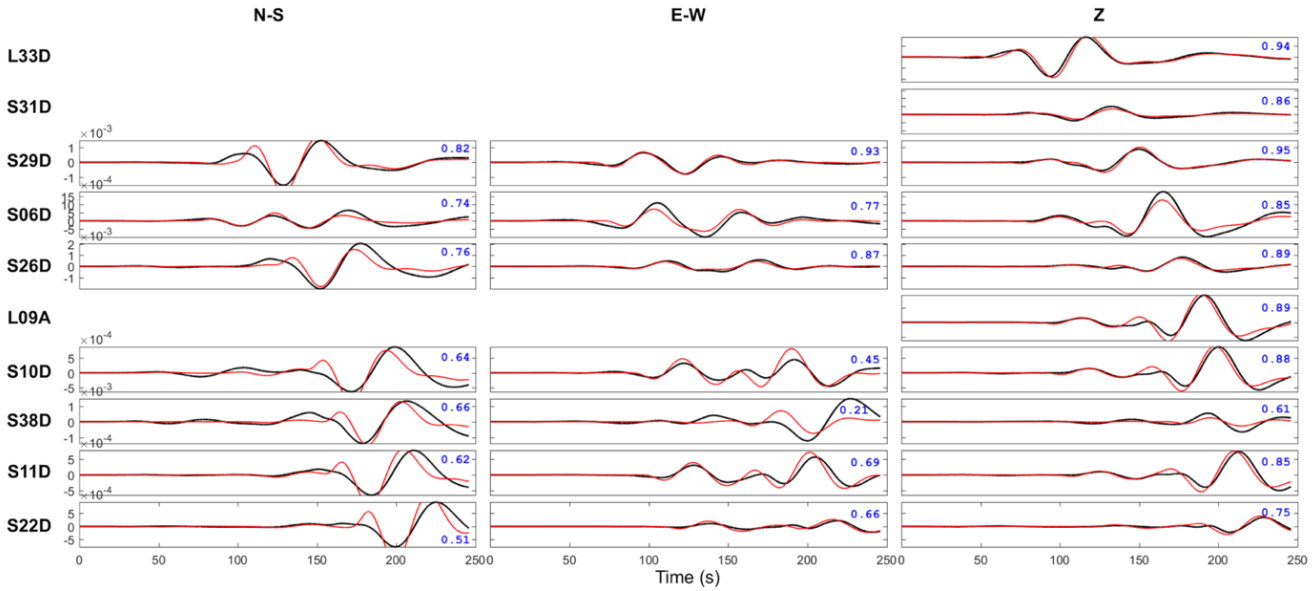

Figure S3: Fits between observed (black lines) and synthetic displacement waveforms (red lines) for the optimum single source low-frequency regional moment tensor of the Romanche earthquake. Waveforms are bandpass filtered between 100 s and 33 s period. Station labels are on the left; component labels along the top. Blue numbers show the variance reduction for each component.

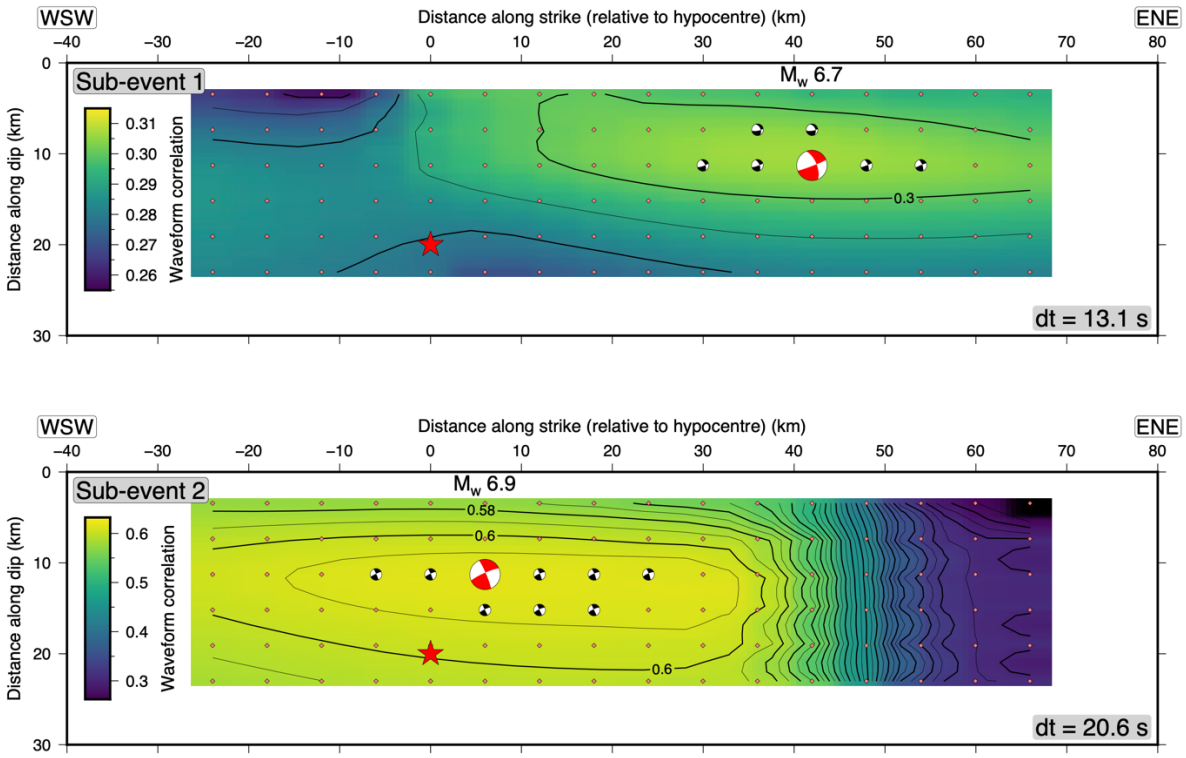

Figure S4: Waveform correlation as a function of trial-point-source position along the fault plane for Sub-Event 1 (SE1; top) and Sub-Event 2 (SE2; bottom). The hypocentre position is given as the red star. The best-fitting regional moment tensor and centroid position is given by the red beach ball. Black beach balls show solutions that have a waveform correlation within 5% of the optimum solution. Diamonds show the location of trial point-sources.

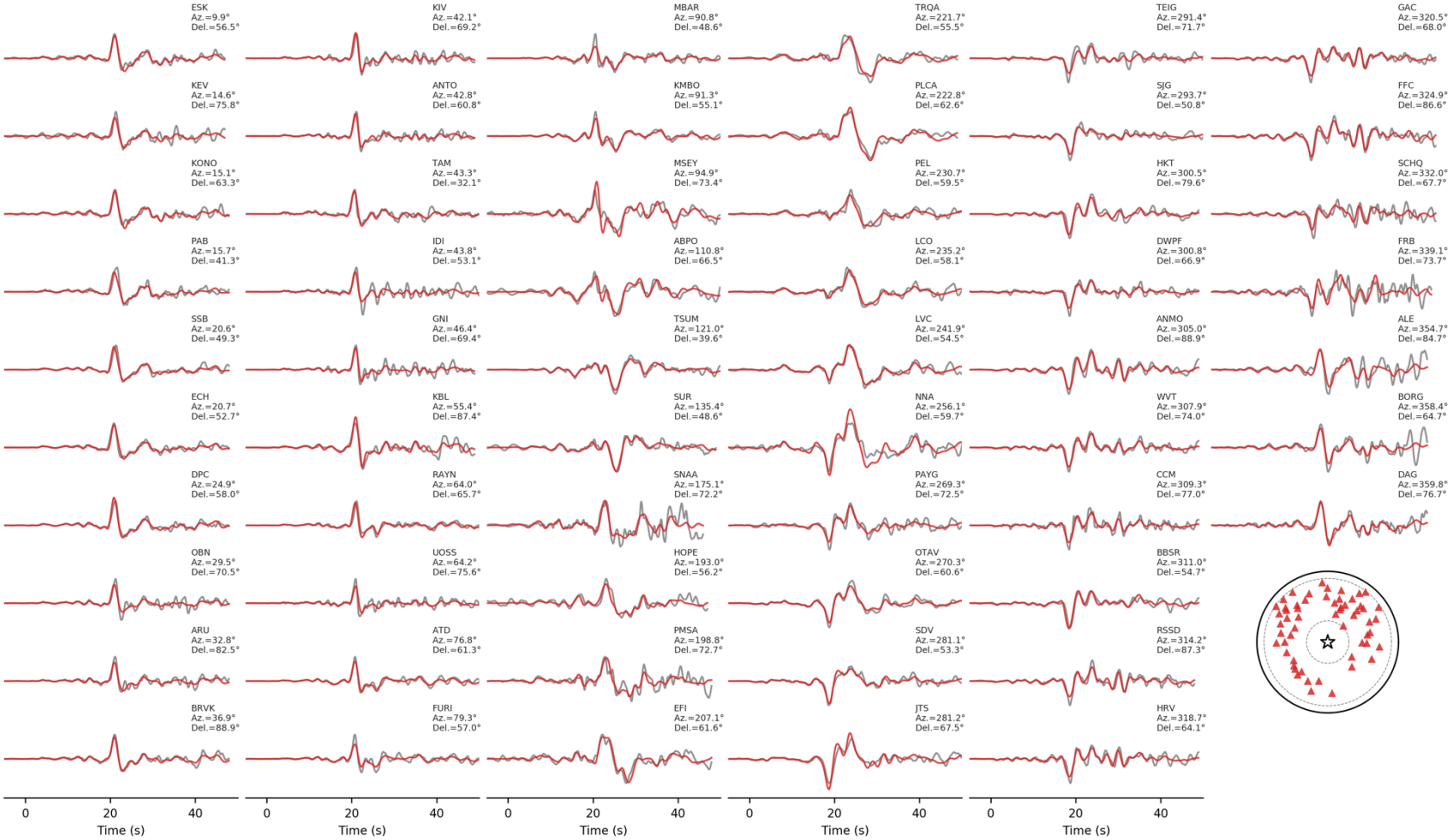

Figure S5: Observed P-waveforms (grey) and synthetic fits (red) for our preferred teleseismic slip model. Right bottom panel is the station distribution. The star and triangles correspond to the epicentre and stations, respectively. Dashed lines are epicentral distances at 30° and 90°.

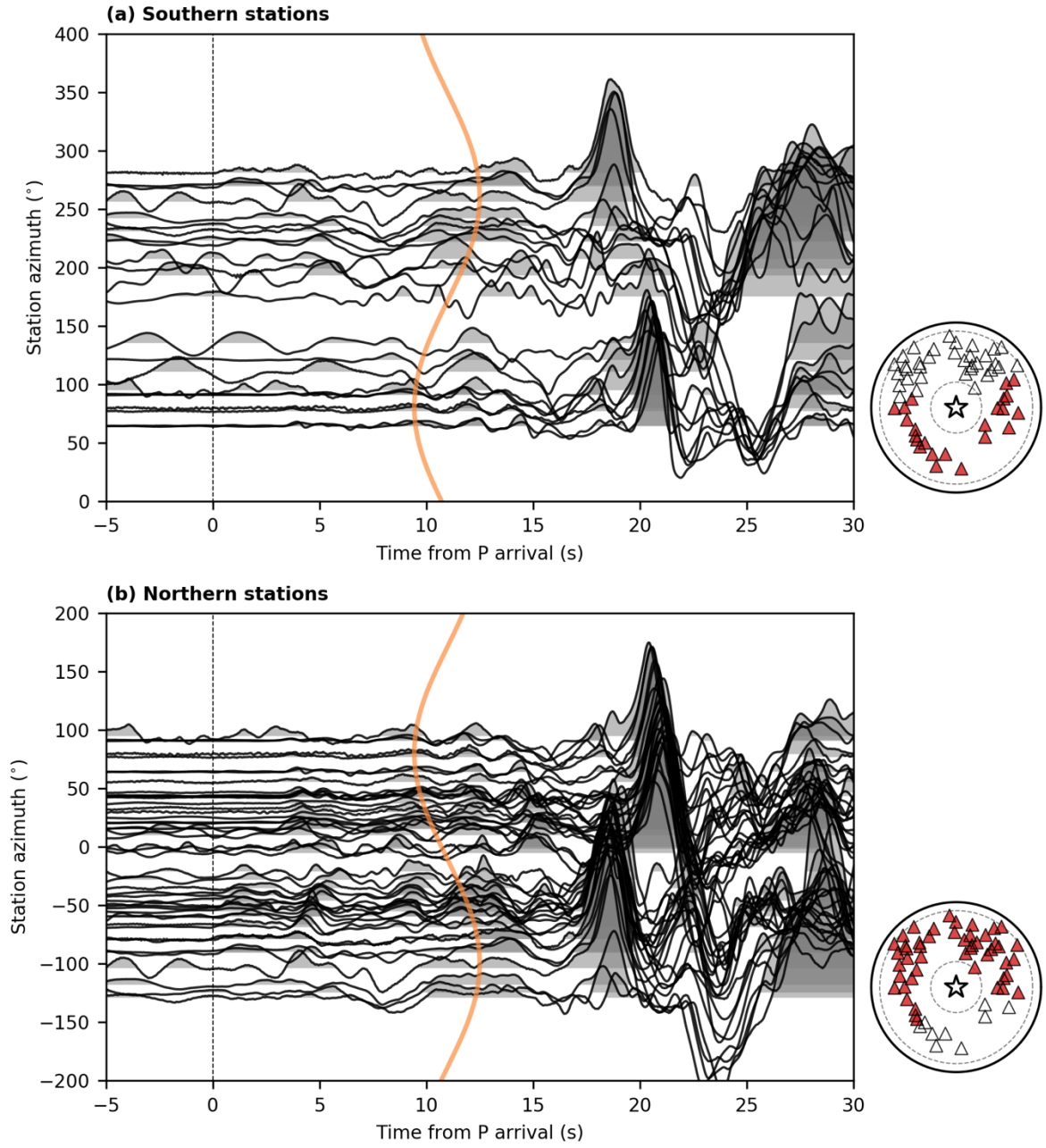

Figure S6: Raw P-wave velocity waveforms plotted versus azimuth. The traces are aligned by P-wave arrival with polarity flipped, and each trace is normalized by its maximum amplitude. Vertical curve is an expected rupture duration[10,11] of SE1, assuming rupture length for 32.9 km toward 80.4° azimuth from the epicentre with rupture speed at 3 km/s. The averaged apparent velocity was assumed to be 21.5 km/s calculated with TauP Toolkit[11]. Inset shows the station distribution. Red triangles are stations shown in each panel. Star is the epicentre. Dashed circles are epicentral distances at 60° and 90°.

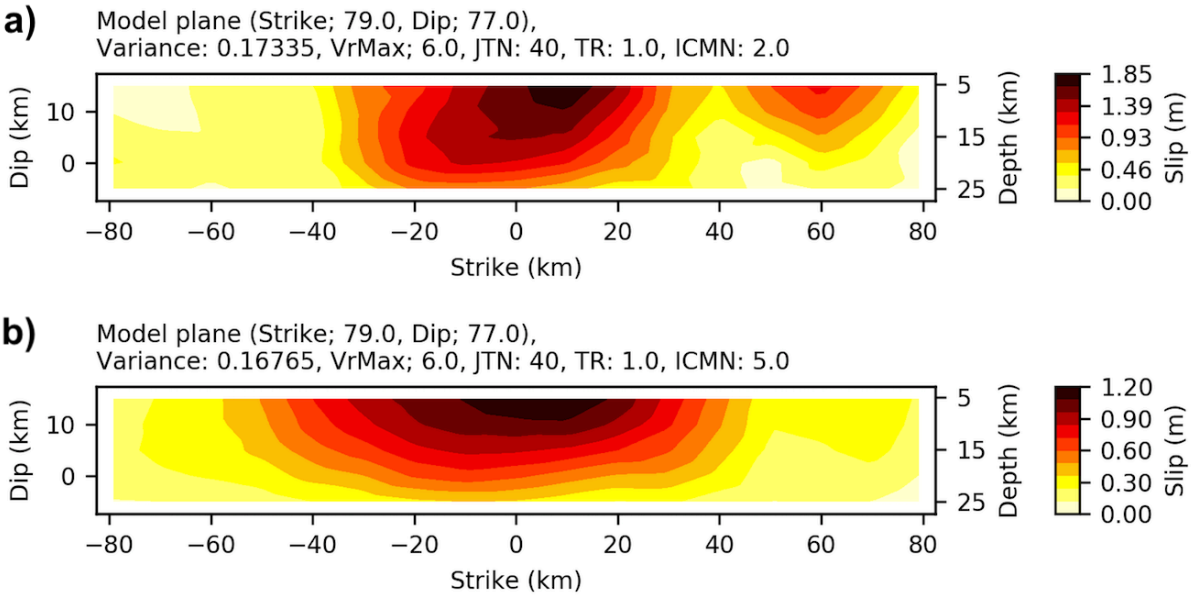

Figure S7: Comparison in the time-integrated slip model between an inversion a) in which the double-couple mechanism of each sub-fault is pre-determined by the model geometry; and b) in which each sub-fault's double-couple mechanism is allowed to vary. Parameters above each panel are as follows. Strike and Dip are geometry of model plane. Variance shows fitting between observed and synthetic waveforms. VrMax is an assumption of maximum rupture velocity that determines the edge of model space where the following slip is represented. JTN is a number of B-spline that forms slip-rate function (if TR is 1.0, then the duration of slip-rate function is 40 s). TR is the time interval (sec) of slip-rate function. ICMN is a flag of model flexibility: if 2.0, the slip is represented as two-basis double couple components (fixed model), and if 5.0, the slip is represented by five-basis double couple components (non-fixed model).

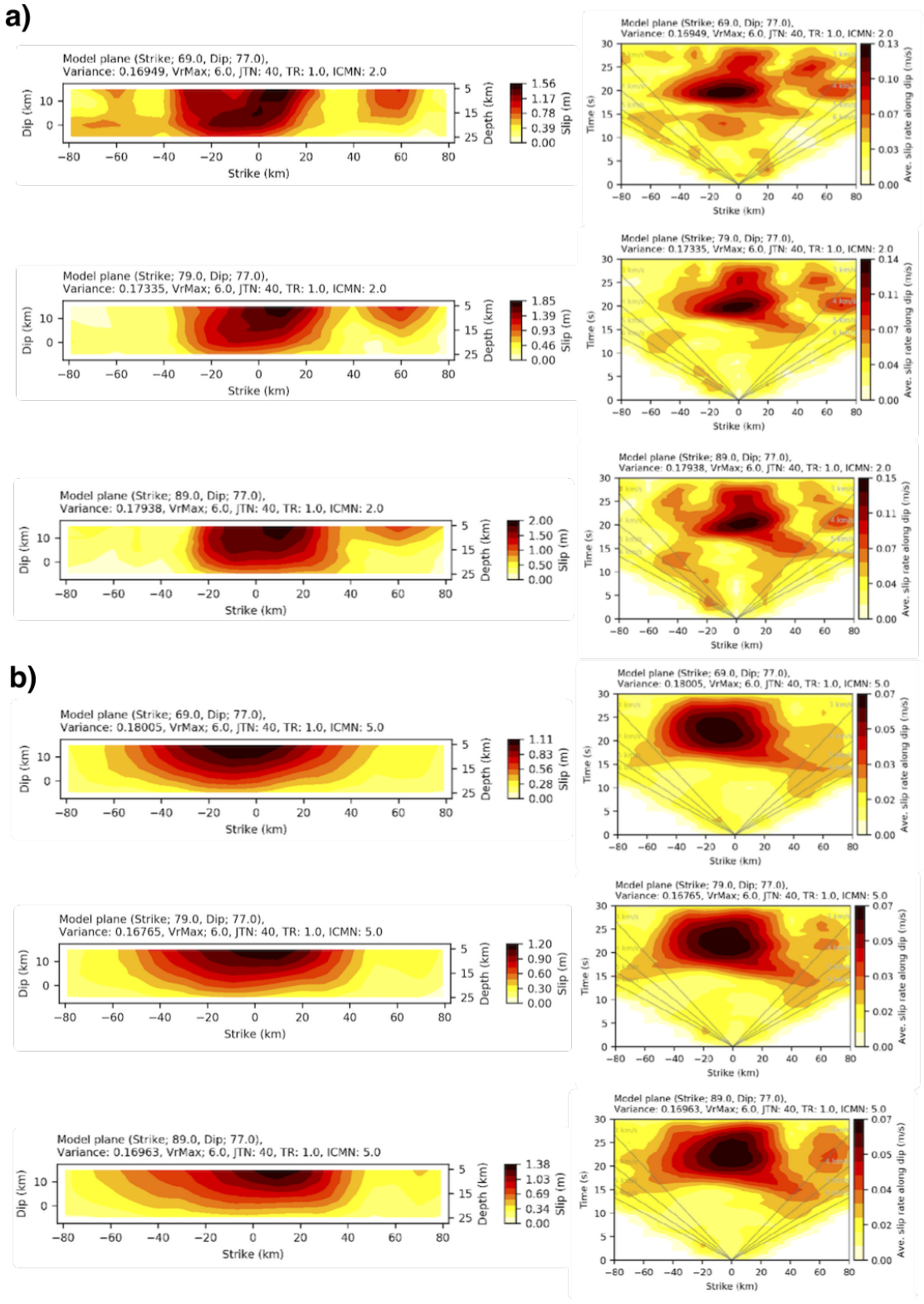

Figure S8: Effect of varying fault strike angle by ±10° for a) assuming slip vectors equal to the prescribed fault plane, and b) using flexible slip vectors. The panels on the left show the time-integrated slip distribution; the panels on the right show the slip-rate evolution as a function of distance along strike and time. The assumed fault geometry is given in the text above each panel.

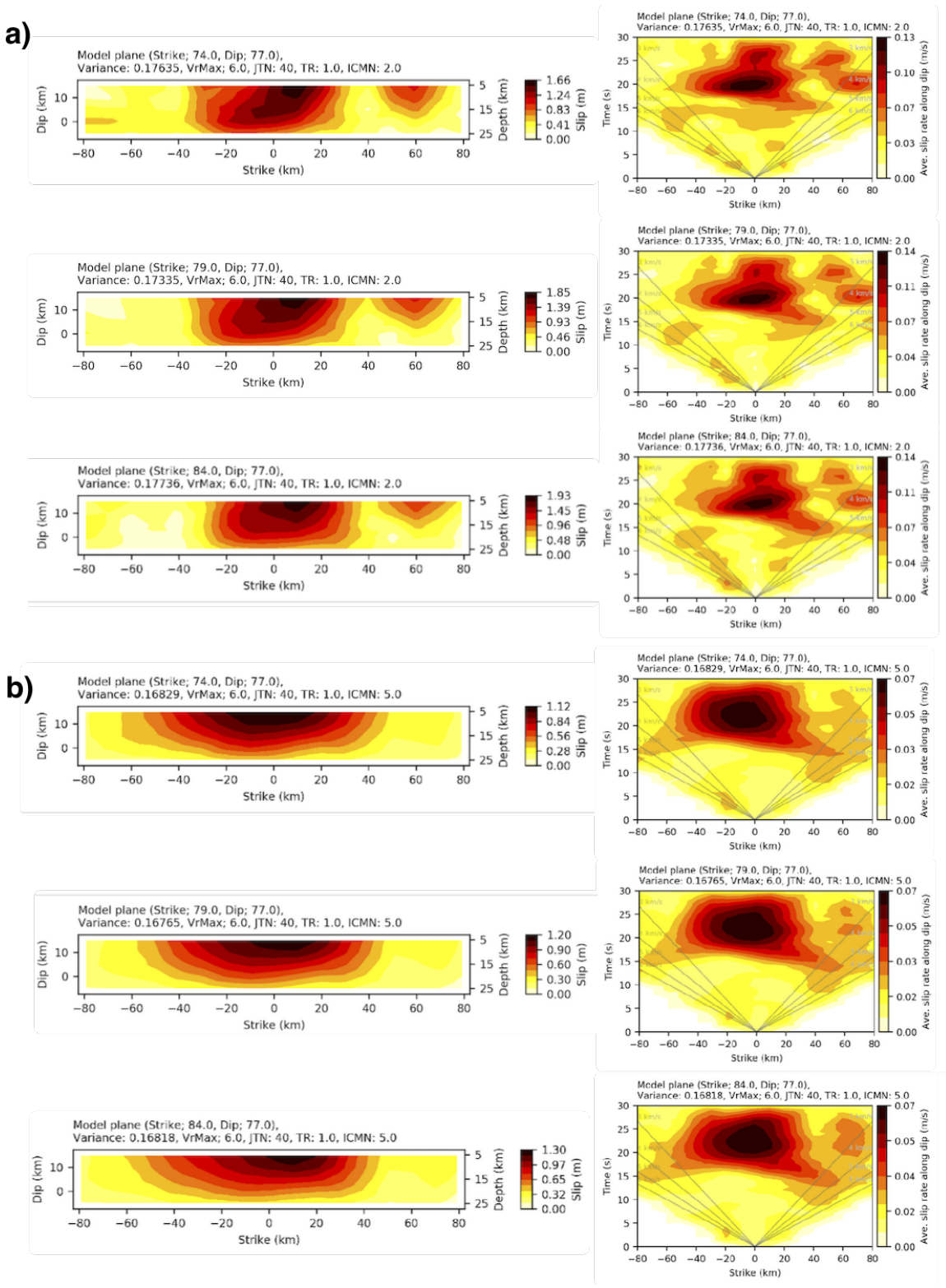

Figure S9: Effect of varying fault strike angle by ±5° for a) assuming slip vectors equal to the prescribed fault plane, and b) using flexible slip vectors. The panels on the left show the time-integrated slip distribution; the panels on the right show the slip-rate evolution as a function of distance along strike and time. The assumed fault geometry is given in the text above each panel.

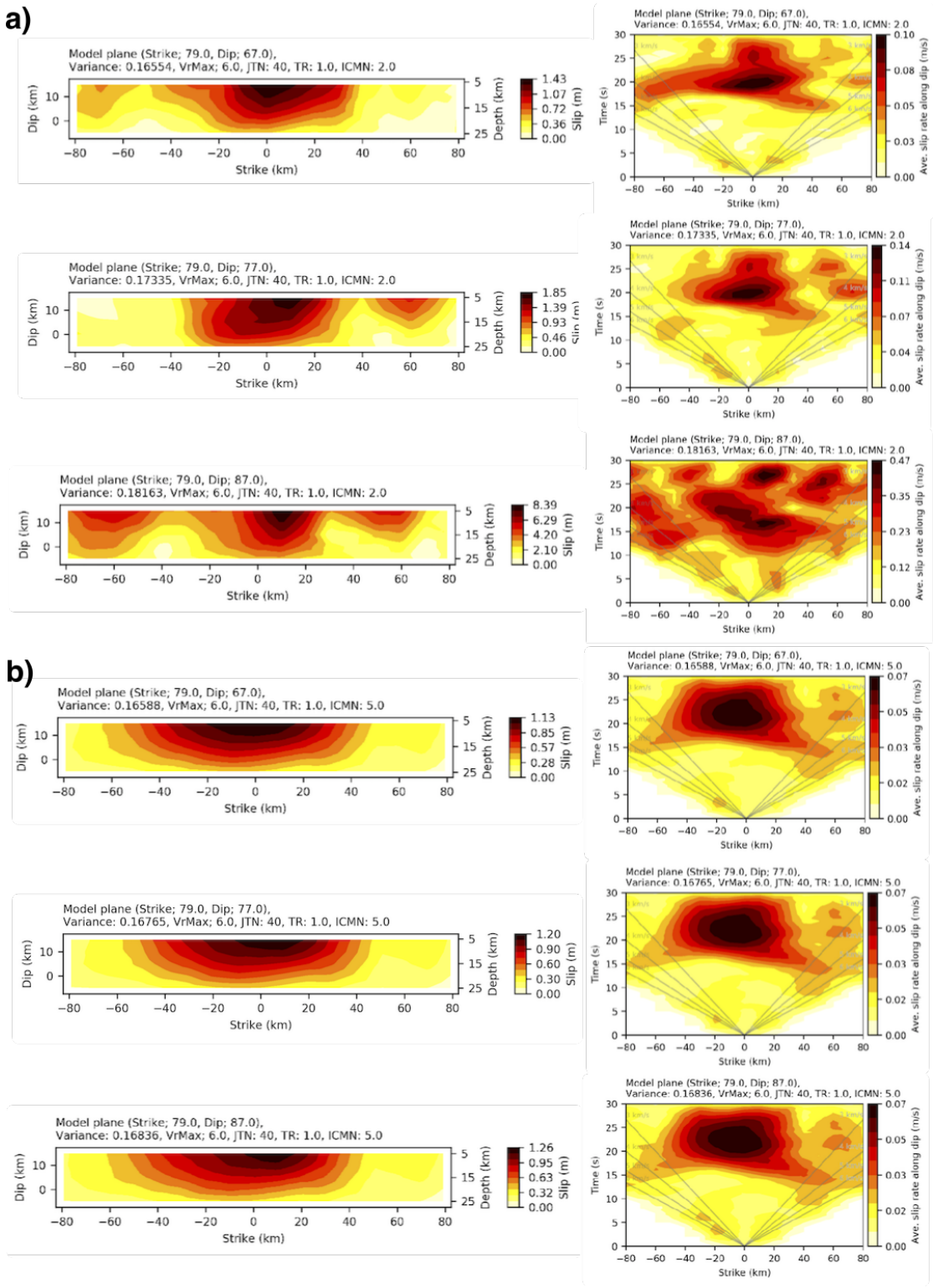

Figure S10: Effect of varying fault dip angle by ±10° for a) assuming slip vectors equal to the prescribed fault plane, and b) using flexible slip vectors. The panels on the left show the time-integrated slip distribution; the panels on the right show the slip-rate evolution as a function of distance along strike and time. The assumed fault geometry is given in the text above each panel.

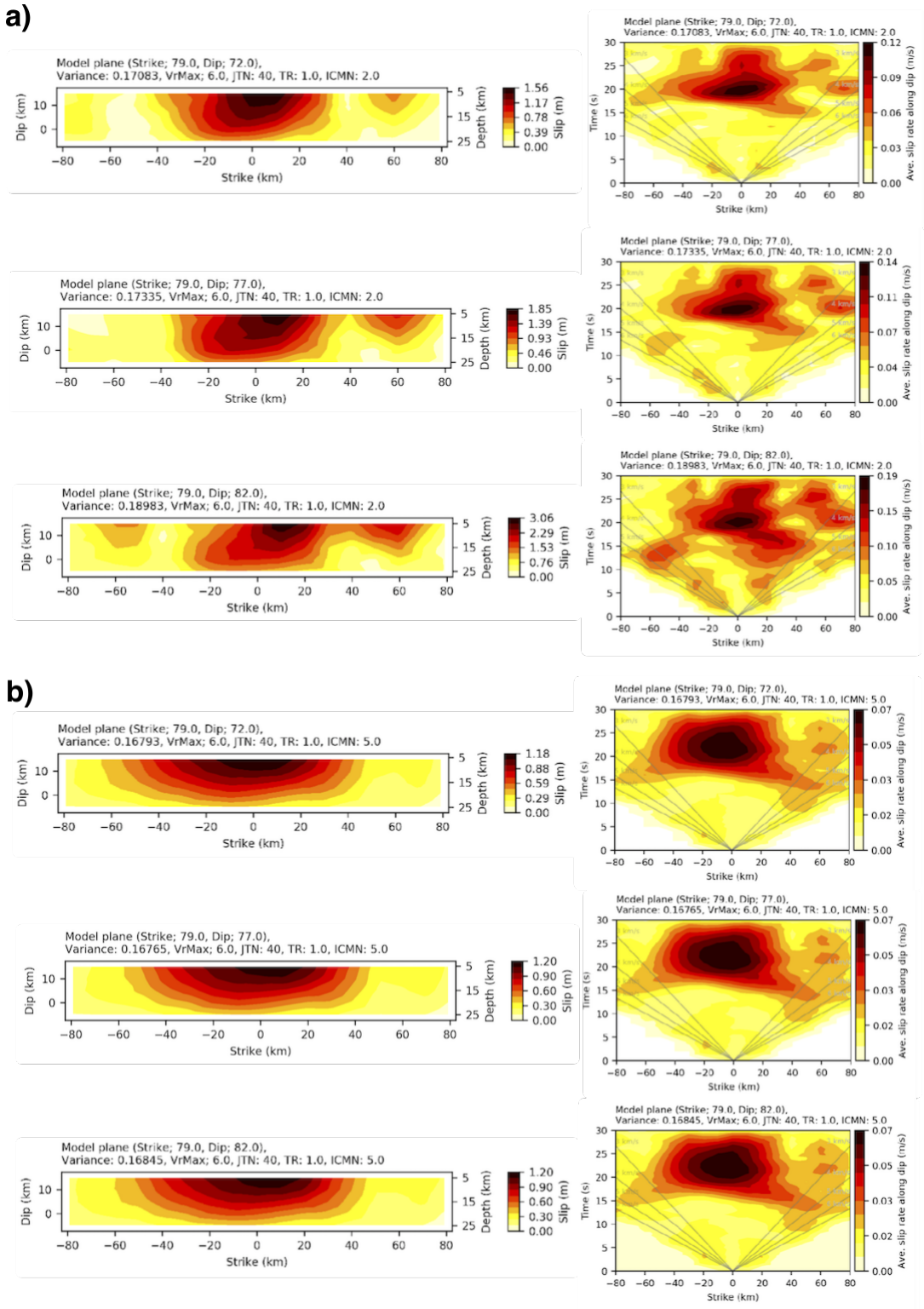

Figure S11: Effect of varying fault dip angle by ±5° for a) assuming slip vectors equal to the prescribed fault plane, and b) using flexible slip vectors. The panels on the left show the time-integrated slip distribution; the panels on the right show the slip-rate evolution as a function of distance along strike and time. The assumed fault geometry is given in the text above each panel.

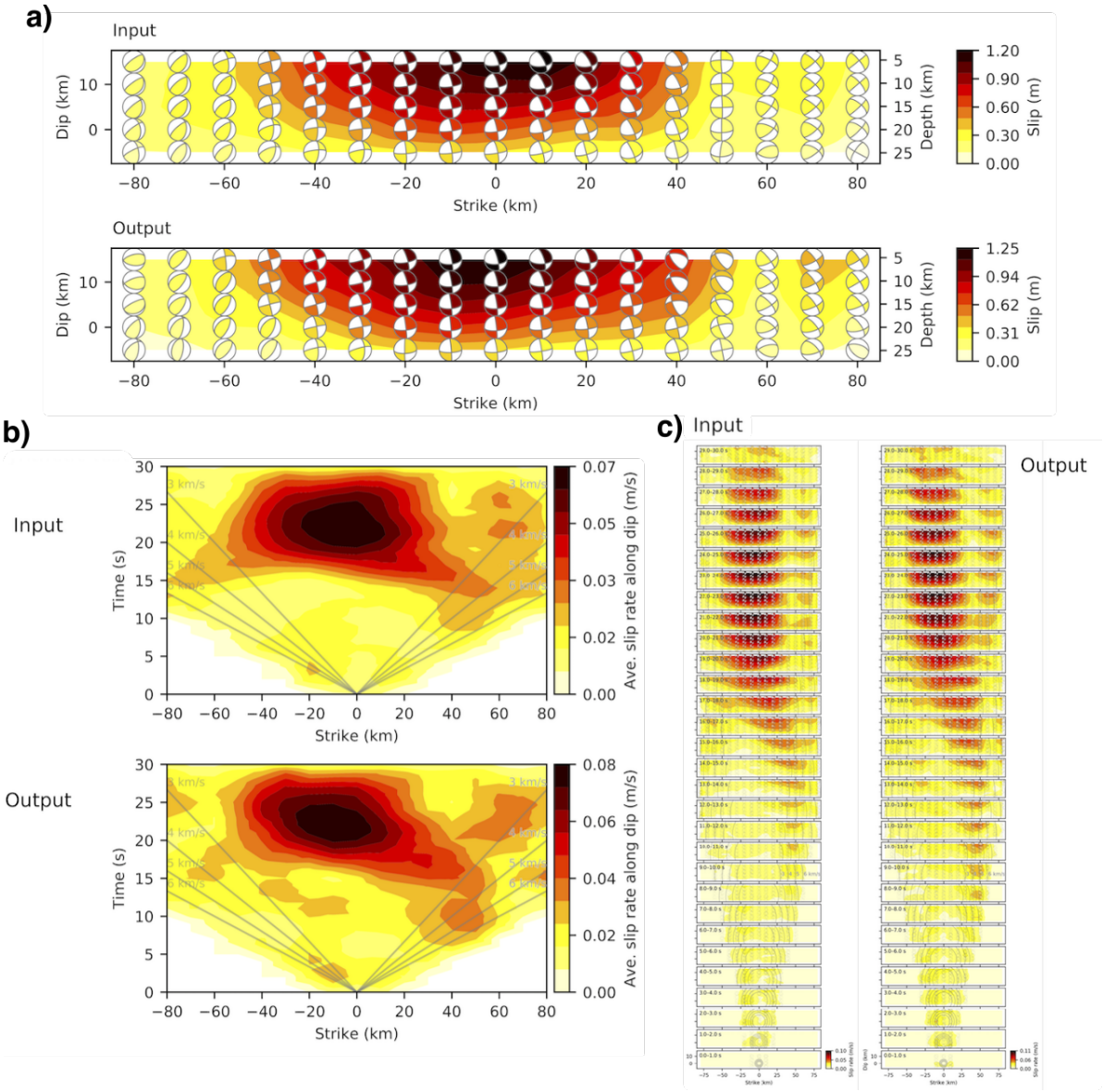

Figure S12: Synthetic test using our optimum teleseismic slip model for the Romanche earthquake as input. a) Time-integrated slip model; b) evolution of slip rate over time and distance along the fault; c) time snapshots showing the 2-D evolution of slip rate.

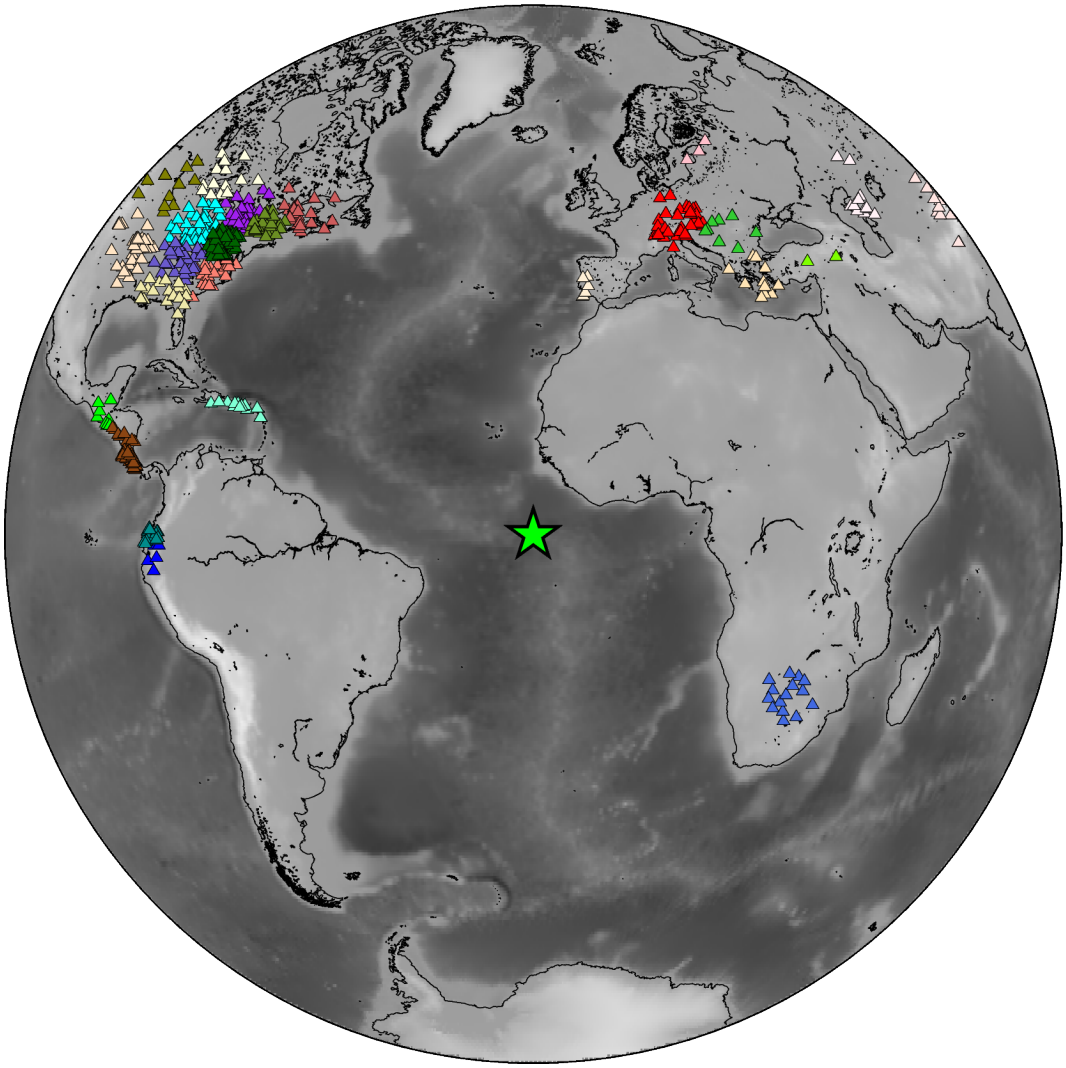

Figure S13: Locations of stations (triangles) in sub-arrays used for the back-projection imaging. Each sub-array has been assigned a unique colour. The green star shows the epicentre of the Romanche mainshock.

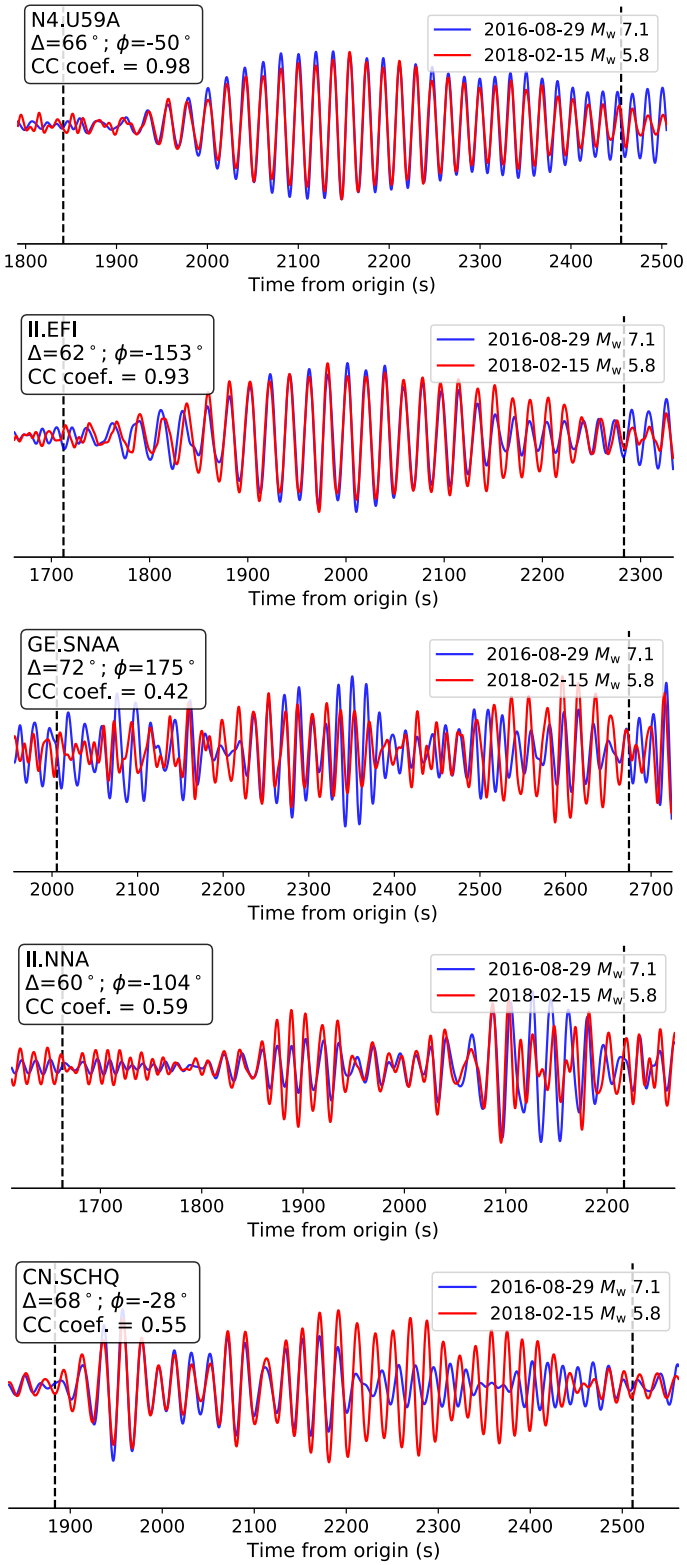

Figure S14: Rayleigh wave vertical displacement seismograms of the M_w 7.1 Romanche mainshock and M_w 5.8 co-located aftershock. The top-left box indicates the network code, station name, epicentral distance, azimuth relative to rupture direction, and cross-correlation value. The locations of these stations are shown in Figure 3b.

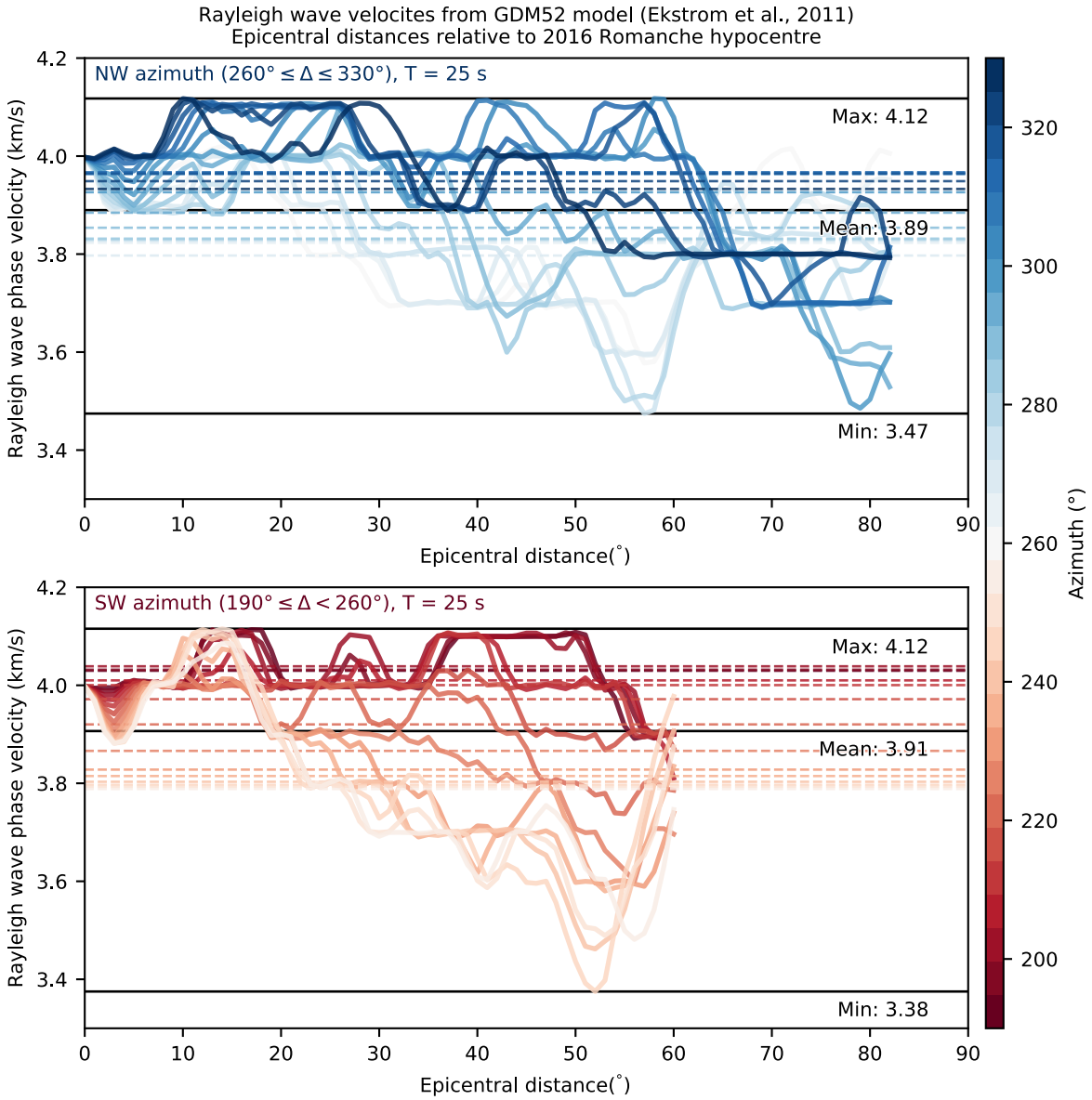

Figure S15: Predicted Rayleigh wave phase velocities along source-station paths for north-westerly azimuths (top) and south-westerly azimuths (bottom) at periods of 25 s from the GDM52 model[12].

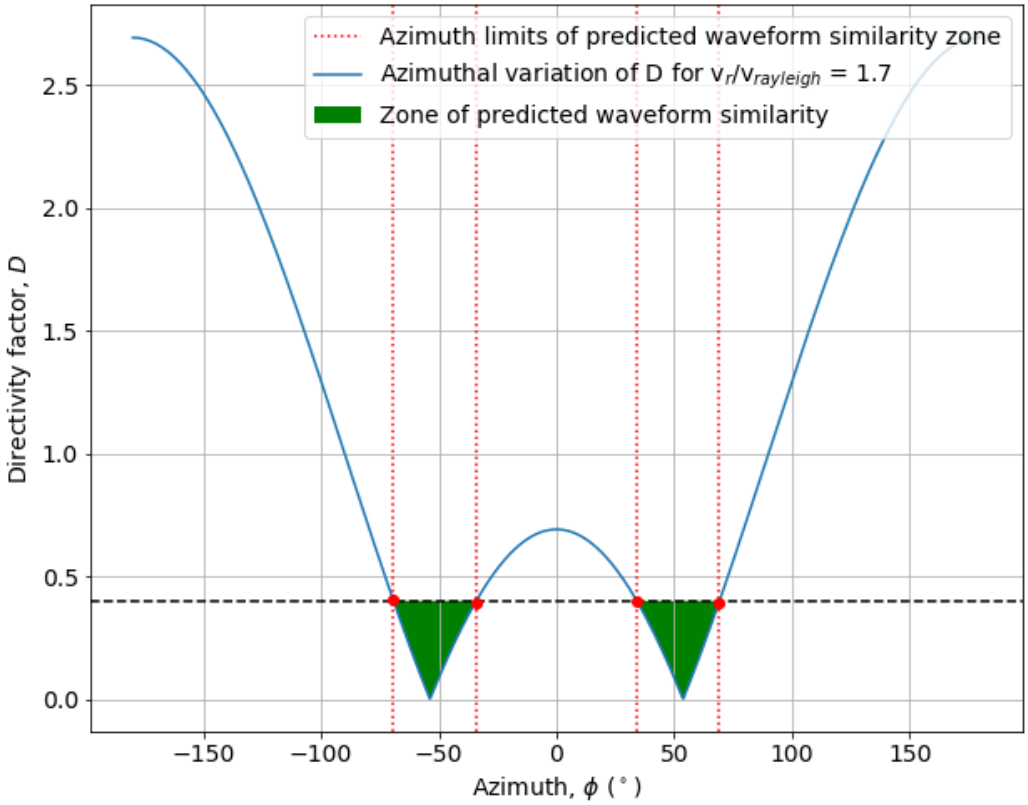

Figure S16: Predicted azimuthal dependence of directivity factor (blue line) for a rupture velocity of 5.7 km/s, period of 10 s, rupture duration of 25 s and Rayleigh wave velocity of 3.4 km/s. The black-dashed line, red dashed lines, and green shaded areas demarcate azimuths where high waveform similarity between the Romanche mainshock and co-located aftershock can be found. These azimuth values correspond well to the locations where high waveform similarity is observed in the data (**Figure 3b**).

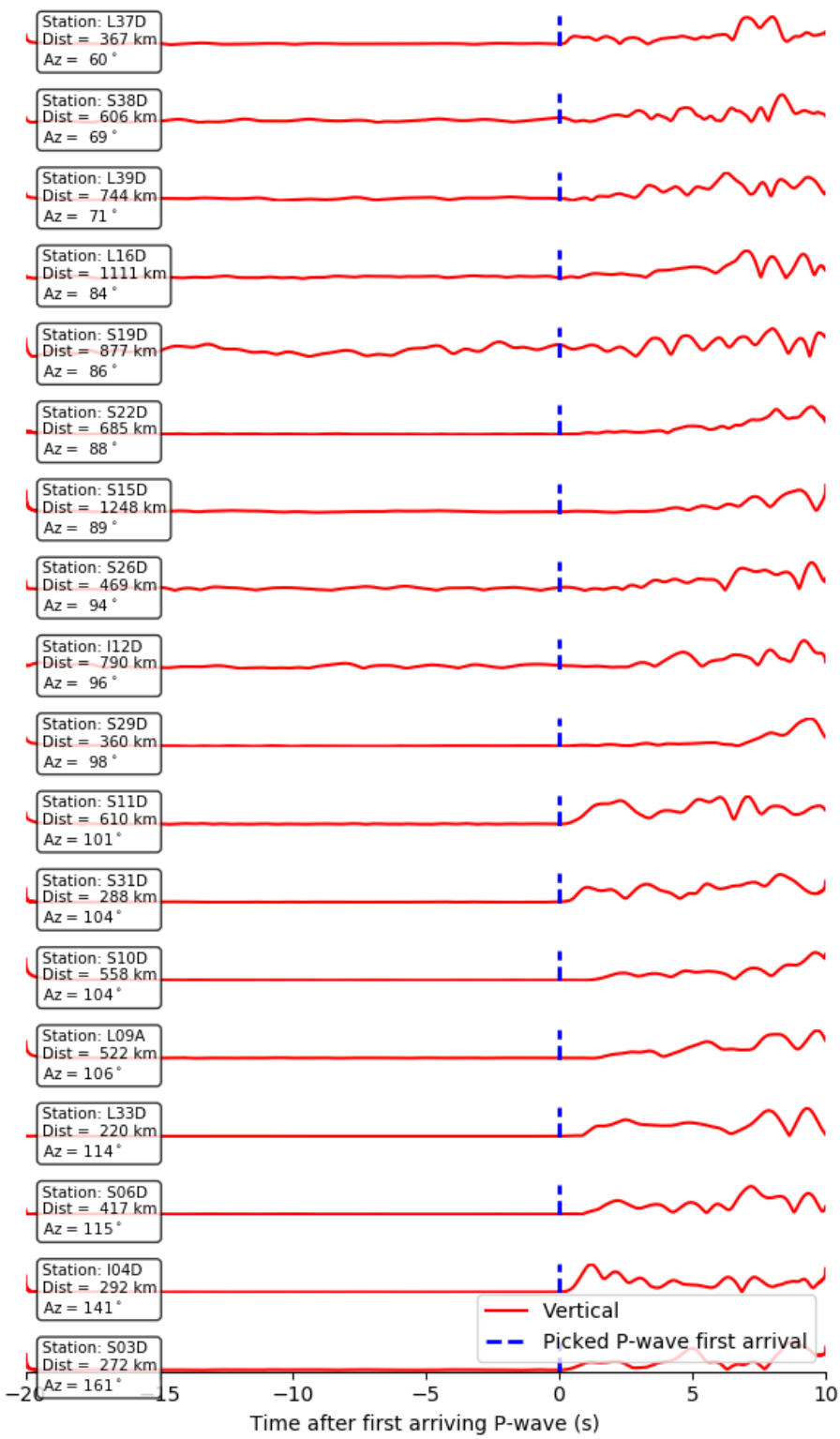

Figure S17: Velocity waveform envelopes bandpass filtered between 0.4 and 1.5 Hz showing the first 10 s of seismic radiation from the Romanche rupture. Waveforms are aligned to the first picked P-wave arrival.

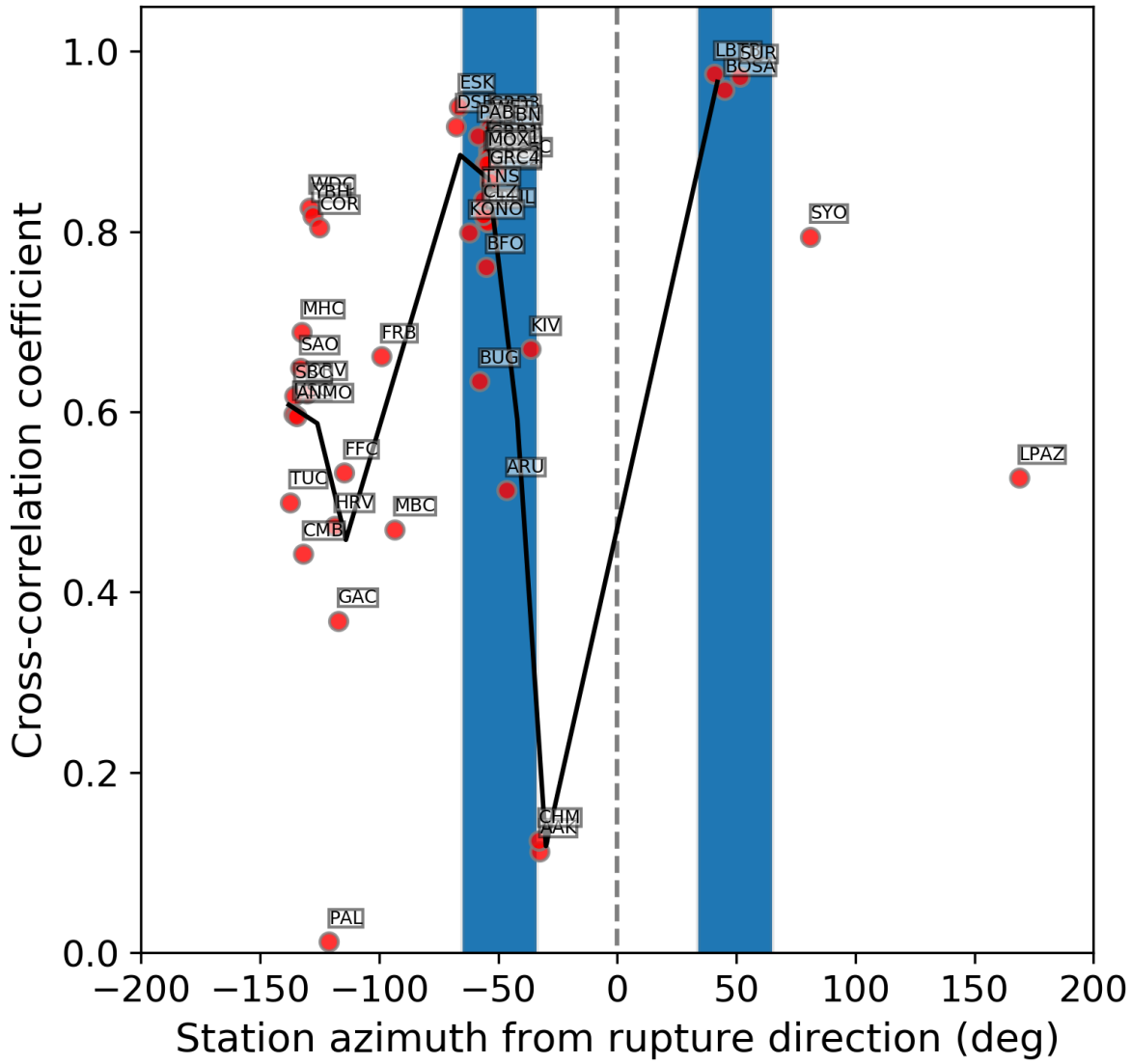

Figure S18: Rayleigh wave cross-correlation values for the 1994 M_w 7.1 Romanche earthquake and a co-located M_w 6.3 earthquake on 1996-11-28.

Supplementary tables

Table S1: Hypocentre estimates for the Romanche mainshock

Hypocentre source / reporting agency	**Latitude**	**Longitude**	**Depth (km)**	**Horizontal distance to our optimum epicentre (km)**
This study (using phase arrivals on OBSs)	0.092°S	17.825°W	23	-
NEIC-USGS	0.046°S	17.826°W	10	3.1
ISC-EHB	0.085°S	17.788°W	10	6.1
GFZ-GEOFON	0.060°S	17.780°W	17	6.9
GEOSCOPE (IPGP)	0.072°S	17.814°W	16	3.0

Table S2: Double-couple percentages from different single-source CMT estimates.

Source	**Double-couple percentage**
This study (low frequency single-point source CMT)	98.7%
GFZ-GEOFON	99.7%
GCMT	77.9%
USGS-NEIC	76.9%

Supplementary Files

- **FileS1_RMT_sourceparameters.xlsx** – Microsoft Excel compatitble spreadsheet containing full source parameters of the single- and multi-point source RMT inversions.
- **FileS2_back_projection_movie_semblance_2.5km.mp4** – Movie showing the evolution of semblance from teleseismic back projection imaging.
- **FileS3_BP_subarrays.dat** – Text file containing the station locations of sub-arrays used for teleseismic back projection imaging.
- **FileS4_MACH_results.dat** – Rayleigh wave cross-correlation results for all stations used in the Mach cone analysis.

References

1. Doran, A. K. & Laske, G. Ocean-Bottom Seismometer Instrument Orientations via Automated Rayleigh-Wave Arrival-Angle Measurements. *B. Seismol. Soc. Am.* **107**, 691 708 (2017).

2. Agius, M., Harmon, N., Rychert, C., Tharimena, S. & Kendall, J. -M. Sediment Characterization at the Equatorial Mid-Atlantic Ridge From P-to-S Teleseismic Phase Conversions Recorded on the PI-LAB Experiment. *Geophys. Res. Lett.* **45**, 12,244-12,252 (2018).

3. Hicks, S. P., Rietbrock, A., Ryder, I. M., Lee, C.-S. & Miller, M. Anatomy of a megathrust: The 2010 M8.8 Maule, Chile earthquake rupture zone imaged using seismic tomography. *Earth. Planet. Sci. Lett.* **405**, 142 155 (2014).

4. Lomax, A., Michelini, A. & Curtis, A. Earthquake location, Direct, Global-search Methods. *Encyclopedia of complexity and systems science* 2449 2473 (2009) doi:10.1007/978-0-387-30440-3_150 .

5. Roessler, D. *et al.* Cluster-search based monitoring of local earthquakes in SeisComP3. *AGU Fall Meeting Abstracts* (2016).

6. Myers, S. C., Johannesson, G. & Hanley, W. A Bayesian hierarchical method for multiple-event seismic location. *Geophys. J. Int.* **171**, 1049 1063 (2007).

7. Bakun, W. H. & Joyner, W. B. The ML scale in central California. *Science* **74**, 1827 1843 (1984).

8. Sokos, E. N. *et al.* Asperity break after 12 years: The Mw6.4 2015 Lefkada (Greece) earthquake. *Geophys. Res. Lett.* **43**, 6137 6145 (2016).

9. Yagi, Y. & Fukahata, Y. Introduction of uncertainty of Green's function into waveform inversion for seismic source processes. *Geophys. J. Int.* **186**, 711 720 (2011).

10. Ammon, C. J. *et al.* Rupture process of the 2004 Sumatra-Andaman earthquake. *Science* **308**, 1133 1139 (2005).

11. Fan, W. & Shearer, P. M. Detailed rupture imaging of the 25 April 2015 Nepal earthquake using teleseismic P waves. *Geophys. Res. Lett.* **42**, 5744–5752 (2015).

12. Ekström, G. A global model of Love and Rayleigh surface wave dispersion and anisotropy, 25–250 s. *Geophys. J. Int.* **187**, 1668–1686 (2011).